Stabilization of Super Electrophilic Pd^{+2} Cations in Small-Pore SSZ-13 Zeolite

Konstantin Khivantsev[1][§], Nicholas R. Jaegers[1,2][§], Iskra Z. Koleva[3][§], Hristiyan A. Aleksandrov[3][*], Libor Kovarik[1], Mark Engelhard[1], Yong Wang[1,2], Georgi N. Vayssilov[3], and Janos Szanyi[1][*]

[1]Institute for Integrated Catalysis, Pacific Northwest National Laboratory Richland, WA 99352 USA

[2]Voiland School of Chemical Engineering and Bioengineering, Washington State University, Pullman, WA 99163 USA

[3]Faculty of Chemistry and Pharmacy, University of Sofia, 1126 Sofia, Bulgaria

*corresponding authors' email addresses: HAA: haa@chem.uni-sofia.bg, JSz: Janos.Szanyi@pnnl.gov

[§] these authors contributed equally KK, NRJ, IZK

Abstract: We provide the first observation and characterization of super-electrophilic metal cations on a solid support. For Pd/SSZ-13 the results of our combined experimental (FTIR, XPS, HAADF-STEM) and density functional theory study reveal that Pd ions in zeolites, previously identified as Pd^{+3} and Pd^{+4}, are in fact present as super electrophilic Pd^{+2} species (charge-transfer complex/ion pair with the negatively charged framework oxygens). In this contribution we re-assign the spectroscopic signatures of these species, discuss the unusual coordination environment of "naked" (ligand-free) super-electrophilic Pd^{+2} in SSZ-13, and their complexes with CO and NO. With CO, non-classical, highly positive [Pd(CO)$_2$]$^{2+}$ ions are formed with the zeolite framework acting as a weakly coordinating anion (ion pairs). Non-classical carbonyl complexes also form with Pt^{+2} and Ag$^+$ in SSZ-13. The Pd^{+2}(CO)$_2$ complex is remarkably stable in zeolite cages even in the presence of water. Dicarbonyl and nitrosyl Pd^{+2} complexes, in turn, serve as precursors to the synthesis of previously inaccessible Pd^{+2}-carbonyl-olefin [Pd(CO)(C$_2$H$_4$)] and -nitrosyl-olefin [Pd(NO)(C$_2$H$_4$)] complexes. Overall, we show that zeolite framework can stabilize super electrophilic metal (Pd) cations, and show the new chemistry of Pd/SSZ-13 system with implications for adsorption and catalysis.

Introduction: Zeolite-supported transition metals represent an important class of catalysts utilized extensively in the industry: from petroleum refining to emissions control.[1-6] Zeolites are highly crystalline aluminosilicates with well-defined binding sites inside microporous channels/cages of various sizes.[7] We recently demonstrated the preparation of atomically dispersed Pd (and Pt) in a small-pore zeolite SSZ-13 (Si/Al ratio ~6) with loadings up to 2 wt% by a simple method (modified incipient wetness impregnation)[8]. Previous studies suggested that harsh hydrothermal aging is required to atomically disperse Pd ions in SSZ-13 and other zeolites.[57,58] In those studies, however, the as-prepared materials initially contained a significant amount of PdO nanoparticles. Although, aging was suggested to improve the metal dispersion, it does not lead to complete dispersion of Pd because of simultaneous loss of Pd and zeolite dealumination under such harsh conditions. We have also shown that Pd/SSZ-13 with atomically dispersed Pd was capable of simultaneously adsorbing NO and CO from vehicle exhaust streams with unrivaled efficiency under practical conditions (i.e., in the presence of water in the stream) at low temperatures.[8-10] The importance of their adsorption capacity lies in the fact that the current state-of-the-art selective catalytic reduction (SCR) materials[61] cannot effectively convert NOx to N$_2$ under practical conditions at temperatures lower than 200 ºC. To circumvent this problem, Pd/SSZ-13 can be used as a low temperature passive NOx adsorber (PNA). In this process NOx is adsorbed at low temperature during cold start/vehicle idle and released at temperatures above 300 ºC,[8] when downstream SCR catalyst composed primarily of Cu/SSZ-13 (previously characterized extensively using various spectroscopic and DFT methods)[61-63] becomes active. Their unique performance for PNA applications, coupled with their excellent hydrothermal stability puts Pd/SSZ-13 at the forefront for low-temperature emission control applications. Furthermore, the high loading of atomically dispersed Pd serves as a perfect example to investigate and understand the behavior of transition metal ions in microporous materials. tThe high uniformity of atomically dispersed Pd ions in the micropores of this zeolite allows us to investigate the fundamentals of NOx uptake and release, and the oxidation state of the metal. Moreover, the ability to synthesize M/SSZ-13 materials with uniform, atomic metal dispersion opens a new avenue to investigate other transition metal ion exchanges zeolites, e.g., Pt and Ag.

The oxidation state of Pd in zeolites has been considered a settled matter for the last three decades. For example, Bell and co-workers[11] concluded that Pd/ZSM-5 with 0.44 wt% loading could be prepared by ion-exchange of oxidized Pd. The IR spectra of adsorbed CO on this sample displayed numerous bands besides the C-O stretching features of Pd^0-CO species: Pd^{+2}-CO, Pd^{+1}-CO and even bands attributed to Pd^{+3}(CO)$_2$ were observed. Subsequently, Hadjiivanov and co-workers[12] concluded that adsorption of CO at 100 K produces Pd^{3+}(CO)$_2$ complexes (unselectively) as well as a range of Pd^{+2}(CO)x, Pd^{+1}-CO and Pd^0-CO complexes upon warming from 100 to 298 K. These studies suggested that Pd is initially present as either Pd^{+4} or Pd^{+3} ions that are reduced to Pd^0 metal upon CO adsorption. However, as mentioned earlier, strategies employed in most previous works to produce atomically monodisperse Pd species were not successful and, as a result, both Pd ions and polynuclear PdO moieties co-existed in the micropores accompanied by larger PdO particles on the external surface. Surprisingly, only one density functional theory (DFT) study has been employed for Pd/zeolite systems, reported by us earlier.[8] Prior to our studies on Pd(Pt)/SSZ-13, high loadings of atomically dispersed metals at elevated levels (> 1%) had not been attained. For example, Moliner et al. demonstrated a route to introduce 0.23 wt% atomically dispersed Pt in SSZ-13 with Si/Al ratio 7

to 9.[13] Here we report the results of a combined spectroscopy/microscopy/computation study on a 1 % Pd loaded SSZ-13 zeolite in which the metal ions are present in atomic dispersion. Here we identify super-electrophilic metal ions in a solid support with the help of FTIR spectroscopy (coupled with DFT calculations) and, quasi in-situ XPS spectroscopy. This latter technique showed an unprecedented 2.3 eV shift of the binding energy (BE) of Pd(II) ion upon dehydration compared to the atomically dispersed partially hydrated ion. This unusually high shift allows us to quantify super-electrophilicity quantitatively : shifts higher than 2 eV upon dehydration of a partially hydrated, atomically dispersed metal cation in zeolite would mean it forms a super electrophilic M cation. This finding can be extended to other metals in zeolites (*vide infra*), and efforts are underway in our group to highlight the unusual catalytic chemistry of such unique super electrophilic as well as highly electrophilic metal fragments.[64] For example, such fragments were recently shown to be exceptionally active for homolytic activation of the C-H bond of ethylene (22 kJ/mole stronger than methane C-H bond at RT) under ambient conditions.[64]

We also highlight that zeolitic confined micropore architecture is imperative for the formation of such super electrophilic species. that do not form selectively (on regular solid, non-microporous/non-zeolitic supports. For example, the high-lying IR bands for the complexes of CO with super electrophilic transition metal ions (stable.g., Pd(II)(CO)$_2$ and Pt(II)(CO)$_2$ complexes) form in zeolites with high yields, but not on any other commonl solid supports like alumina, zirconia, silica etc.

The interaction of these super-electrophilic Pd cations with CO results in the formation of non-classical carbonyl complexes. Similar complexes are also observed with Pt^{2+} and Ag$^+$ ions in SSZ-13.

Experimental: Na-SSZ-13 with Si/Al = 6 and ion-exchanged twice with 2 M NH$_4$NO$_3$ aqueous solution at 80 °C for 3 hours yielding the ammonium forms of SSZ-13. NH$_4$-SSZ-13 was subsequently dried under ambient conditions and then at 80 ºC. Samples with 0.1 and 1 wt% Pd, 1 wt% Pt and 3 wt% Ag loadings were prepared by modified ion exchange (for Pd and Pt) with 10 wt% Pd(NH$_3$)$_4$(NO$_3$)$_2$ solution (Sigma-Aldrich 99.99%) with NH$_4$-SSZ-13, and platinum(II) tetraamine nitrate solution, and regular ion exchange for AgNO$_3$ (99.99%) solution with H-SSZ-13 (produced by decomposition of NH$_4$-SSZ-13 in air at 550 °C). More specifically, minimum amount of the Pd(II) or Pt(II) precursor solution was added to zeolite in the amount approximately equivalent to the total pore volume of the zeolite. The thick paste was mixed and stirred vigorously for 30 minutes, followed by calcination in air at 650 °C for 5 h (ramping rate 2 °C/min) in case of Pd and 350°C in case of Pt. H-forms of zeolites could be used as well with identical results: in that case, Pd and Pt tetramine salts were dissolved in the minimum amount of dilute ammonium hydroxide solution (pH=11.5), mixed with zeolite to form thick paste (mixed vigorously), followed by drying and calcination in air at 650 °C for Pd and 350 °C for Pt. In the case of Ag, 1 g of H-SSZ-13 was dispersed in water and stirred with ~20 ml of 0.1 M silver nitrate solution for 3 hours; then the sample was purified by 5 successive centrifugation-redispersion cycles and dried at 80 ºC overnight. To avoid silver auto-reduction under high vacuum in the FTIR cell, the sample was heated to 180 °C to remove residual water from Ag/SSZ-13 as quickly as possible and then immediately cooled down prior to IR measurements.

The in situ static transmission IR experiments were conducted in a home-built cell housed in the sample compartment of a Bruker Vertex 80 spectrometer, equipped with an MCT detector and operated at 4 cm^{-1} resolution. The powder sample was pressed onto a tungsten mesh which, in turn, was mounted onto a copper heating assembly attached to a ceramic feedthrough. The sample could be resistively heated, and the sample temperature was monitored by a thermocouple spot welded onto the top center of the W grid. The cold finger on the glass bulb containing CO was cooled with liquid nitrogen to eliminate any contamination originating from metal carbonyls, while NO was cleaned with multiple freeze–pump–thaw cycles. Prior to spectrum collection, a background with the activated (annealed, reduced or oxidized) sample in the IR beam was collected. Each spectrum reported is obtained by averaging 256 scans.

HAADF-STEM was used to probe the dispersion of Pd and Pt in prepared samples. The analysis was performed with a FEI Titan 80-300 microscope operated at 300 kV. The instrument is equipped with a CEOS GmbH double-hexapole aberration corrector for the probe-forming lens, which allows for imaging with 0.1 nm resolution in scanning transmission electron microscopy mode (STEM). The images were acquired with a high angle annular dark field (HAADF) detector with inner collection angle set to 52 mrad.

Standard NOx adsorption tests were conducted in a plug-flow reactor system with powder samples (120 mg, 60–80 mesh) loaded in a quartz tube, using a synthetic gas mixture that contained ~200 ppm of NOx or (200 ppm of NOx, 200 ppm CO, 3 vw% H$_2$O and 14% O$_2$) balanced with N$_2$ at a flow rate of 310 sccm (corresponding to 330,000 h^{-1}).

All the gas lines were heated to over 100 °C. Concentrations of reactants and products were measured by an online MKS MultiGas 2030 FTIR gas analyzer with a gas cell maintained at 191 °C. Two four-way valves were used for gas switching between the reactor and the bypass. Prior to storage testing at 100 °C, the sample was pretreated in 14% O$_2$ balanced in N$_2$ flow for 1 h at 550 °C and cooled to the target temperature in the same feed. The gas mixture was then switched from the reactor to the bypass, and 200 ppm of NOx was added to the mixture. Upon stabilization, the gas mixture was switched back from bypass to the reactor for storage testing for 10 min. The sample was then heated to 600 °C at a rate of 10 °C/min to record the desorption profiles of gases in the effluent.

To further disprove the possibility of formation of Pd(IV) species upon calcination in oxygen, we performed the following experiment. In a quartz reactor equipped with valves at both ends ~ 300 mg of 1 wt% Pd/SSZ-13 was heated in dry oxygen at 600 °C for 3 hours. After cooling it down to room temperature in dry air flow, the reactor was purged with dry nitrogen. Then we moved the reactor to a moisture and oxygen-free glove box without exposure to ambient air (there the sample was also pre-vacuumed in the antechamber of the glovebox under high vacuum 10^{-5}-10^{-6} Torr.)The pink powder of Pd/SSZ-13 from the reactor was then transferred into a 20 ml vial with a septum screw-cap. With a syringe a 1ml gas-phase sample from that vial was injected it in the GC. The analysis of the gas phase confirmed the absence of any oxygen.

Then, through the septum, we introduced a small amount of pure de-aerated H$_2$O into the vial containing the dry dehydrated catalyst. The sample turned yellow, characteristic of hydrated Pd(II) ions. If during the interaction with water the reduction of Pd(IV) to Pd(II) were indeed to take place, then the following red-ox reaction would occur: Pd(IV) + 2 e →

Pd(II). If Pd accepts two electrons, water has to give electrons which can only occur via: $H_2O - 2e \rightarrow 2H^+ + 1/2O_2$. If Pd(IV) were indeed reduced to Pd(II), this process would produce 14 micromoles of O_2. In the ~20 ml vial, this amount of oxygen would be equivalent to ~0.3% of oxygen by volume easily detectable with a GC. We injected 1 ml of the gas-phase from the closed vial (after water exposure) and observed no oxygen in the gas phase. Thus, no oxygen was produced, and no Pd(IV) was formed during Pd/SSZ-13 heating in oxygen.

XAS spectra were collected at X-ray beamline 9-1 of the Argonne National Laboratory. The storage ring electron energy was 7 GeV and the ring current was in the range of 495-500 mA. Prior to these measurements, each powder sample was loaded into a cell. The XAS data were collected in the fluorescence mode. Samples were scanned at energies near the Pd *K* absorption edge (24,350 eV). Standards (PdO, Pd foil and $K_2[PdCl_6]$ were scanned as well. PdO and $K_2[PdCl_6]$ were mixed with BN prior to scanning). 1 wt% Pd/SSZ-13 sample in Fig. S1 was calcined in air in the XAS cell at 350 °C for 1 hour, then cooled down in the air flow and XANES recorded at room temperature.

X-ray Photoelectron Spectroscopy (XPS) experiments were performed using a Physical Electronics Quantera scanning X-ray microprobe. This system uses a focused monochromatic Al Kα X-ray (1486.7 eV) source for excitation and a spherical section analyzer. The instrument has a 32 element multichannel detection system. The 80 W X-ray beam focused to 100 μm diameter was rastered over a 1.1 × 0.1 mm rectangle on the sample. The X-ray beam was incident normal to the sample and the photoelectron detector was at 45° off-normal. High-energy-resolution spectra were collected using a pass-energy of 69.0 eV with a step size of 0.125 eV. Note that the samples experienced variable degrees of charging. Low-energy electrons at ~1 eV, 20 μA and low-energy Ar$^+$ ions were used to minimize this charging. First, the 0.1 and 1 wt% Pd samples were measured as is. The samples then were heated in 10% O_2/He for 1 h at 600 °C (ramping rate 10 °C/min), followed by cooling down in O_2/He to room temperature in a flow cell attached to the XPS system. The pretreated samples were immediately transferred into the UHV chamber without exposure to the open air for the first XPS analysis. Note that following the heating treatment, adventitious carbon, ideal for binding energy (BE) calibration, became absent. Therefore, all binding energies were referenced to a Si 2p BE of SSZ-13 of 102.7 eV.

Results and Discussion: After calcination in O_2 (at 400 °C) the K-edge EXAFS (XANES region) of our atomically dispersed 1% Pd in SSZ-13 showed that all Pd is in the +2 oxidation state.[8] Comparison of the XANES region of Pd/SSZ-13 spectrum with those of PdO, $[Pd(NH_3)_4](NO_3)_2$, and standard $[Pd(IV)Cl_6]^{2-}$ clearly shows the absence of Pd(IV) species within the margin of EXAFS sensitivity (Fig. S1). The only other stable compounds in which Pd^{+4} and Pd^{+3} are known to exist are $Zn_2Pd(IV)O_4$ and $LaPd(III)O_3$ produced by high-temperature, high-pressure, solid-state synthesis. The XANES region K-edge features of these compounds are caused by the splitting of the d-levels of Pd^{+4} and Pd^{+3} in the octahedral crystal field, dissimilar to Pd/SSZ-13 calcined in air.[14] A series of FTIR spectra collected from our atomically dispersed 1wt% Pd/SSZ-13 sample upon dosing CO at 298 K is displayed in Fig. 1. (The cryo HAADF-STEM images for this sample, confirming atomic dispersion of Pd, are provided in SI (Fig. S2).)
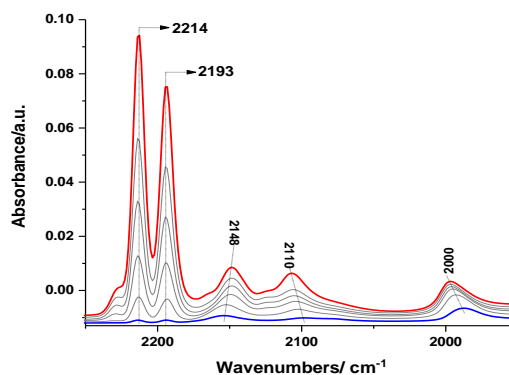

Figure 1. FTIR spectra of adsorbed CO at 298 K on 1 wt% Pd/SSZ-13 with Si/Al=6. (CO was introduced into the IR cell in a stepwise fashion; $P(CO)_{max}$~5 Torr); the lines between the blue spectrum (first CO pulse) and the red spectrum (final state) indicate sequential adsorption of approximately equal aliquots of CO until the desired CO amount is dosed on the sample (spectra are presented in similar fashion all throughout the text). Please note that we chose 1 wt% Pd/SSZ-13 with Si/Al=6 as a model for our study due to the high uniformity of atomically dispersed Pd(II) species that are stabilized selectively as Pd(II)/ 2Al by proximal Al sites. We have also explored the effect of Si/Al ratio on the speciation and FTIR during CO adsorption on Pd/SSZ-13 with the same Pd loading (1 wt%) and varied Si/Al ratios of 12 and 30 (Figs S33 and S34, the discussion regarding the effect of Si/Al ratio on the Pd speciation and uniformity is in the captions for Figs S33 and S34).

Upon CO adsorption at room temperature, well-defined absorption bands develop. The major doublet bands are centered at 2214 and 2193 cm^{-1}. Minor features at 2148 and 2110 cm^{-1} belong to CO on ionic Pd^{+2} species (see Tables S1,S2 for DFT confirmation). The bands at 2090 cm^{-1} and below represent CO bound to metallic Pd. Aleksandrov, et al.,[15,16] demonstrated for Pt clusters that the decrease in coordination number (CN) by 1 corresponded to a downshift of approx. ~7 cm^{-1} in agreement with experimental studies.[17] The fact that the metallic ~1990 cm^{-1} band lies below that of larger (>3 nm) Pd nanoparticles (~2090 cm^{-1}) means that small Pd$_4$-Pd$_6$ clusters are present and possibly formed during CO adsorption. To further confirm this observation, part of the Pd was reduced *in situ* with CO at 400 °C prior to CO adsorption. The IR spectra showed an increase in the intensity of the 1990 cm^{-1} band. Upon vacuum-induced desorption, the center of this band red-shifted due to the elimination of dipole-dipole coupling interactions present at higher coverages (Fig. S3). As such, we ascribe the peak at ~1990 cm^{-1} to CO adsorbed linearly on small Pd clusters, whereas bands below 1900 cm^{-1} represent doubly- and possibly triply-bridged CO on such clusters that are formed in small amounts (<0.5% of total Pd). Note that in agreement with works by Stair and co-workers[42] and Hadjiivanov and co-workers[43], the molar extinction coefficients of CO bands for CO-containing species dramatically increases as the υ$_{CO}$ goes down. For example, for metallic Pt-bound CO, it was found that the 2090 cm^{-1} band has >8 times higher molar extinction coefficient than the 2110 cm^{-1} belonging to ionic Pt.

The 2214 and 2193 cm^{-1} bands belong to **v**$_{C-O}$ vibrations previously assigned to Pd(III)(CO)$_2$ complexes by the Bell group[11] and later Hadjiivanov group[12] on Pd/ZSM-5. Unlike those systems in which CO adsorption produced a wealth of species, in our 1 wt% Pd/SSZ-13 (Si/Al=6) these species are

formed selectively (>90%) at room temperature. These $Pd(CO)_2$ species are stable in the presence of CO, O_2 or inert atmosphere, and fully decompose only above 140 ºC. This means that the high uniformity of Pd in small-pore SSZ-13 enables the selective production of this species. Indeed, the symmetric and asymmetric CO bands grow and, upon evacuation, disappear in concert (Fig.1, Fig. S3), suggesting they belong to the same species. The assignment of these bands to dicarbonyls of Pd is further confirmed by isotopic labeling of the adsorbate (^{13}CO) (Fig. S4). In contrast, the stabilization of the Pd^{+3} in zeolite would require at least 3 Al atoms in either 6-membered or 8-membered rings of the SSZ-13 structure (which is highly unlikely) or Pd^{+3}-OH fragment held by 2 proximal Al atoms. To explain the observed high wavenumbers, we modeled unique $Pd^{4+}(CO)_2(O)$ and $Pd^{3+}(CO)_2(OH)$ complexes (Tables 1 and S1). In the case of $Pd^{4+}(CO)_2(O)$ spontaneous formation and desorption of carbon dioxide is observed. The calculated vibrational frequencies of the other complex, $Pd^{3+}(CO)_2(OH)$, were notably lower than 2200 cm^{-1}: 2141 and 2114 cm^{-1}. The structure of Pd(IV) was more stable with 0 unpaired electrons and for this reason, we included it. In that case CO_2 molecule leaves the complex. These results do not agree with the experimental data. Additionally, $Pd^{+1}(CO)_2$ complex (1 unpaired electron) has calculated symmetric and asymmetric C-O stretching vibrations at 2103 and 2063 cm^{-1}, significantly lower than the observed values.

Structures	BE	BE$_{L1}$	BE$_{L2}$	v(L)^a	N$_s$
Pd^+					1
$Pd^+(CO)$	-158			2075	1
$Pd^+(CO)_2$	-252	-94		2103;2063	1
$Pd^+(CO)_3$	-273	-20		2098;2058;2055	1
Pd^{2+}					0
$Pd^{2+}(CO)$	-87			2114	0
$Pd^{2+}(CO)_2$	-215	-128		2172;2138	0
$Pd^{2+}(CO)_3$					
$Pd^{2+}(CO)_{4zeo}$	-271			2178;2133;2122;1845	0
$Pd^0(CO)_{4\ desorbed}$				2119;2073;2068;2012	
$Pd^{2+}(CO)(OH)$		-187		2121	0
$Pd^{2+}(CO)_2(OH)$		-262		2165;2125	0
$Pd^{2+}(CO)(C_2H_4)$	-209	-151	-98	2140	0
$Pd^{3+}(CO)(OH)$		-117		2158	1
$Pd^{3+}(CO)_2(OH)$		-160		2141;2114	1
$Pd^{4+}(CO)_2(O)$	0				
$Pd^{2+}(O)Pd^{2+}$					0
$Pd^{2+}(CO)(O)Pd^{2+}(CO)$	-321			2132/2116	0

Table 1. Binding energies of the neutral ligands (in kJ/mol), vibrational frequencies of diatomic ligands (**v** (L) in cm^{-1}, and number of the unpaired electrons in the systems, N$_s$ for the select Pd carbonyl complexes (All considered structures are summarized in Table S1, not shown in Table1 for brevity).

The positions of the IR features for the $Pd^{2+}(CO)_2$ complex (2214 and 2193 cm^{-1}) lie at much higher values than gas phase CO (by 61 and 50 cm^{-1}, correspondingly) suggesting the identity of a non-classical Pd carbonyl [$Pd(CO)_2$] with essentially no back-donation from Pd to CO.[19] For an otherwise classical $Pd(CO)_2$ complex with Pd back-donation, CO vibrational frequencies are expected to be much lower. Indeed, for a classical square-planar Rh(I)(CO)$_2$ fragment in zeolite H-FAU (isoelectronic and isostructural with square-planar $Pd^{+2}(CO)_2$ with two framework oxygens as ligands), the CO signatures lie at 2117 and 2053 cm^{-1}, below the gas-phase CO value: in this complex, Rh is tightly bound to the framework. DFT provides remarkable agreement between the calculated and experimental frequencies for this complex.[18,52,54]

Non-classical metal carbonyls have received attention in the organometallic literature. Due to pioneering efforts coming from the Aubke group,[19-23] for example, it was demonstrated that non-classical transition metal carbonyls can be produced from Pd or Pt compounds in toxic/corrosive magic acids HSO_3F/SbF_5 in the absence of moisture and under CO pressures. (As noted by Olah and Klumpp[44] a variety of cationic species from organo-cations to metal cations should be called "superelectrophilic" due to the labile and weakly coordinating nature of fluorosulfonate or similar weakly coordinating anions produced in the "magic"/superacid; moreover, with the help of NMR spectroscopy the organic (carbocationic) isolated super-electrophilic species have been identified in magic acids on the basis of their very high shifts in the 13C NMR region, meaning that extremely positive "super electrophilic" carbocations form under such conditions; however, super-electrophilicty of metal ions/fragments have not been ever proved or quantified before – below, we show we can now quantify it with XPS for the first time). For example, $Pd^{+2}(CO)_2(SO_3F)_2$ was obtained, in which $Pd^{+2}(CO)_2$ fragments were weakly interacting with the anion. On the basis of single-crystal XRD data $Pd^{+2}(CO)_2$ fragments were proposed to stabilize via secondary contacts of CO with basic SO_3F groups dispersed in the crystallographic structure. These compounds were stable only in the complete absence of moisture and decomposed immediately in the presence of traces of water or above 130 ºC. The frequencies of the u$_{sym}$ and u$_{asymm}$ vibrational features were observed at 2220 and 2199 cm^{-1} (in solution). Note, that the split between these two bands is identical to that has been previously assigned to Pd(III)(CO)$_2$.[11,12] Thus, we may reassign the 2214 and 2193 cm^{-1} signatures to $Pd^{+2}(CO)_2$ non-classical dicarbonyl, charge-balanced by 2 negative charges associated with Al pairs and weakly interacting with the basic O ions of the zeolite, in principle similar to $Pd^{+2}(CO)_2(SO_3F)_2$. XPS data (*vide infra*) (in addition to EXAFS data showing Pd^{+2} in an oxygen environment) confirm this result. The slight red shift from 2220 to 2214 cm^{-1} reflects either a higher basicity of zeolite oxygens compared with SO_3F anions or, alternatively the effect of confinement. The more correct annotation for this sample would then be a charge-transfer/ion-pair complex between [$Pd(CO)_2$]$^{2+}$ and two $^-$O-Zeolite. Indeed, CO adsorption on the pink-colored $Pd^{2+}(^-$O-Zeo)$_2$ produces a purple-colored [$Pd(CO)_2$]$^{2+}$($^-$O-Zeo)$_2$ complex (Fig. S5) indicating significant charge-transfer in the ~520 nm UV-Vis spectral region of both species. We tried to model this complex with DFT calculations (Table S1, Figs. S6-S9 for structures of various modeled Pd complexes). The results from DFT calculations show significant disagreement with respect to the observed frequencies and in the split between the CO bands. The calculated CO signatures are 2172 and 2138 cm^{-1} with a 34 cm^{-1} split. However, among all $Pd(CO)_2$ fragments this is the only one that shows a C-O stretching vibrational feature above that of gas-phase CO. We have also attempted to model the non-classical complex with the known crystallographic structure (i.e., $Pd^{+2}(CO)_2(SO_3F)_2$). The $Pd(CO)_2(SO_3F)_2$ structure was optimized and the calculated frequencies were 2199

and 2164 cm^{-1}, once again lower than the experimental values of 2220 and 2199 cm^{-1}. The calculated split was 35 cm^{-1}, larger than the experimentally measured split of 20 cm^{-1} (the same as for modeled $Pd^{+2}(CO)_2$ in zeolite). Again, these computational estimates give ~30-40 cm^{-1} lower frequencies than the experiment. We suggest that the non-classical superelectrophilic nature of such Pd complexes complicates their modeling by DFT. However, based on the provided evidence, this Pd/SSZ-13 system selectively forms non-classical $Pd^{+2}(CO)_2$ fragments and not $Pd^{+3}(CO)_2$ as previously proposed in the literature.[11,12,24,28] The non-classical nature of this complex is further indirectly corroborated by the fact that its infrared signature does not depend on zeolite type to any significant extent and presents a $Pd^{+2}(CO)_2$ fragment stabilized as ion pairs (with the Al-associated negative oxygen atoms of zeolite acting as a negative part of the ion pair, whereas Pd^{+2} and $Pd^{+2}(CO)_2$ are the positive +2-charged part of the ion pair) in a small (~0.85 nm) SSZ-13 cage (Fig. S10).[11,12,24] Zeolites with larger cavities do not seem to selectively stabilize this fragment, yet it is observable.[24] In conclusion, semi-free non-classical, superelectrophilic, $Pd^{+2}(CO)_2$ is formed in the micropores of SSZ-13, and is probably stabilized by secondary interactions between its CO ligands and the basic oxygens of zeolite framework. The interactions of CO fragments with framework sites (stabilization) withdraws it from Al and suggests that it may exist as a semi-free $[Pd(CO)_2]^{2+}$ ion weakly interacting with the framework (the framework itself can thus be regarded as a weakly coordinating macro-anion). All other non-classical carbonyl complexes prepared in HSO_3F/SbF_5 exist only in the complete absence of moisture.[19-23] Herein, we demonstrated that a $Pd^{+2}(CO)_2$ non-classical carbonyl complex is insensitive to the presence of H_2O. The IR spectra (Fig. 2, Fig. S11) recorded after the exposure of the $Pd^{+2}(CO)_2$/SSZ-13 to moisture, clearly substantiates the remarkable stability of this complex.
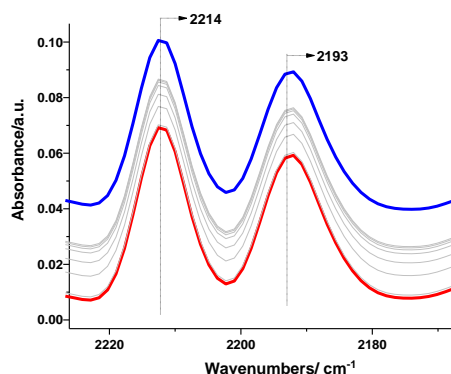

Figure 2. FTIR spectra collected on $Pd^{+2}(CO)_2$/SSZ-13 with Si/Al=6 upon adsorption of H_2O at 298 K. (H_2O was introduced into the IR cell in a stepwise fashion; $P_{H_2O,max}$~6 Torr; sample before H_2O adsorption "dry" – red graph, final state "wet" – blue graph).

The small-pore SSZ-13 structure with ~0.85 nm diameter cages may not provide the typical "liquid" water environment which lends unique stability to this complex (Fig. S10). Furthermore, adsorption of NO pulses on this complex leads exclusively to the formation of $Pd^{+2}(NO)(CO)$ which has been previously characterized in our prior work and identified as the species responsible for the excellent passive NOx adsorber (PNA) performance under practical conditions (Fig S12-14. (CO and NO uptake curves under practically rele-

vant conditions are displayed in Fig. S15 confirming the stoichiometry of the complex in addition to FTIR data in Figs. S12, S14.)[8] Additional experimental evidence of the peculiar chemistry taking place upon dosing only dry NO on Pd(II)/SSZ-13 is provided in Fig. S13 and the corresponding discussion in the caption. As we have previously suggested, based on DFT calculations and deduction from experimental data,[8] the 1865 cm^{-1} band belongs to Pd(II)-NO complex whereas 1806 cm^{-1} band which forms upon NO adsorption is due to reduction of Pd(II) by a free radical NO resulting in the formation of a Pd(I)-NO complex, analogous to what we have shown for the Cu(II)/SSZ-13 system.[65]

The Aubke group has also reported the ability to form a non-classical $[Pd^{+2}(CO)_4]$ complex under higher CO pressures.[19-23] We have therefore modeled two tetracarbonyl complexes of Pd^{2+} cation and of Pd^0 in the CHA structure (Table S1). Interestingly, in the $Pd^{2+}(CO)_{4zeo}$ complex the carbon of one of the CO molecules is bound to an oxygen center from the zeolite with C-O distance of 141 pm. Despite the fact that we were successfully able to model and construct these unusual homoleptic structures, we find no evidence that they are formed under our experimental conditions most likely due to kinetic reasons, i.e. high pressures of CO and different temperatures may be required to observe the formation of such completely homoleptic structures.

We extended our work to 1 wt% Pt and 3 wt% Ag in SSZ-13 (Si/Al = 6) as well (Fig S16 for HAADF-STEM images of 1 wt% Pt/SSZ-13). In Pt/SSZ-13, non-classical $Pt^{+2}(CO)_2$ with CO frequencies 2186 and 2153 cm^{-1} is formed in addition to two classical Pt^{+2}-CO monocarbonyls (Fig. 3). DFT modeling of classical Pt^{+2} monocarbonyl complexes allows us to unambiguously assign the 2133 cm^{-1} band to $Pt^{+2}(CO)$ in the 8-membered ring, whereas the ~2117 cm^{-1} band belongs to $Pt^{+2}(CO)$ in the 6-membered ring (Fig.S17, Tables 2 and S2). These results clearly demonstrate the confinement of isostructural Pt^{+2}-CO which leads to the downshift of its IR signature. These bands cannot belong to the dicarbonyl species because they grow independently from each other. The fact that 2186 and 2153 cm^{-1} bands change in concert upon evacuation is a clear indication that they belong to the same species, which, analogously with $Pd^{+2}(CO)_2$, can be assigned to $Pt^{+2}(CO)_2$. Surprisingly, DFT modeling found two energetic minima for two isostructural and isoelectronic $Pt^{2+}(CO)_2$ complexes in the 8-membered ring with very similar stabilities but different frequencies (2156 and 2108, and 2179 and 2136 cm^{-1}, respectively). The likely reason for this is that in one of the complexes CO molecules are close to the zeolite framework with O-O distances of 240 pm. This unusual finding that two essentially isoelectronic and isostructural M-CO complexes could have significantly different C-O stretching frequencies is notable.

Str.	BE	BE$_{L2}$	x(L)^a	d(Pt-L)	d(Pt-O$_{zeo}$)	N$_s$
Pt^{2+}					206;206;212;212	0
Pt^{2+}(CO)	-134		2108	185	208;211;211	0
Pt^{2+}(CO)$_2$	-318	-184	2182;2136	189;189	209;209	0
Pt^{2+}(OH)				190	202;210;211	1
Pt^{2+}(CO)(OH)	-181		2146	188;194	209;209	1
Pt^{2+} 8 MR					200;206;211	0
Pt^{2+}(CO)_a 8MR	-309		2138	186	202;211;212	0
Pt^{2+}(CO)_b 8MR	-309		2134	186	202;211;213	0
Pt^{2+}(CO)$_2$_a 8MR	-481	-173	2156;2108	190;190	206;210	0
Pt^{2+}(CO)$_2$_b 8MR	-479	-170	2179;2135	189;190	205;210	0

Table 2. Binding energies of all the neutral ligands (BE, in kJ/mol) and of the second adsorbed ligand (BE$_{L2}$, in kJ/mol), vibrational frequencies of diatomic (C-O) ligands (x(L) in cm^{-1}), Pt-ligand distances (in pm) (Pt-L), distances between Pt cation and zeolite O centers (Pt-O$_{zeo}$) and number of the unpaired electrons in the systems, N$_s$.

^{a} the frequencies are shifted by +35 cm^{-1} since the calculated C-O vibrational frequency for a CO molecule in gas phase 2108 cm^{-1} is lower by 35 cm^{-1} with respect to the experimental value 2143 cm^{-1}.

DFT calculations for Pt^{+2}(CO)$_2$ both in 6 and 8-membered rings show better agreement with respect to the symmetric C-O stretch with the experiment (~2180 cm^{-1} both), although the asymmetric C-O stretch at 2135/2136 cm^{-1} is much lower than the observed 2153 cm^{-1}. Moreover, the observed experimental frequencies for Pt^{+2}(CO)$_2$ are below those of Pd^{+2}(CO)$_2$ (which is in *perfect agreement* with the observation by Aubke group, with the split between band for Pt^{+2}(CO)$_2$ (34 cm^{-1}) larger than for Pd^{+2}(CO)$_2$ (21 cm^{-1}).[19-23] Thus, the formation of non-classical Pt^{+2}(CO)$_2$ fragment is confirmed. Although the intensities of the bands belonging to classical Pt monocarbonyls are higher than for the Pt^{+2}(CO)$_2$ species, due to the aforementioned significantly higher molar extinction coefficients of CO complexes with downshifted vibrational frequencies, the Pt^{+2}-CO complexes may not be present as the major species.[42,43,53] Moreover, it is important to note that this is the first observation of Pt^{+2}(CO)$_2$ fragment on a solid support. Non-zeolitic solid support do not seem to provide any evidence for its existence. However, in some previous literature, the Pt^{+2}(CO)$_2$ was claimed to exist in ZSM-5 zeolite (noteworthy, unlike in our case, metal nanoparticles were always present in those systems alongside cationic Pt sites): in one report by Hadjiivanov and co-workers, the 2165 and 2150 cm^{-1} bands with the split between them equal to 15 cm^{-1}, were assigned to Pt^{+2}(CO)$_2$[55]; interestingly, the bands at 2204 and 2168 cm^{-1} in Y-zeolite[56] (in another report by the same group at 2211 and 2175 cm^{-1} in ZSM-5[55], correspondingly) were assigned to Pt^{+3}(CO)2. Based on our new understanding of the system, it is highly unlikely that Pt^{+3} ions would be present in ZSM-5 or Y with Si/Al ratio 10-15 due to the fact that this would require 3 Al sites to be in very close proximity either in the same ring or in nearby rings (although it is possible, statistically, their amount would be very low). In those works the observed split ~34-35 cm^{-1} corresponds exactly to the split we observe for Pt^{+2}(CO)$_2$ fragment confined in SSZ-13. Thus, the signatures

assigned to Pt^{+3}(CO)$_2$ in previous works with split between CO bands of 34-35 cm^{-1} have to be re-assigned to Pt^{+2}(CO)$_2$. The 2165 and 2150 cm^{-1} assigned previously to Pt^{+2}(CO)$_2$, thus, belong to some other Pt carbonyl complexes, and not Pt^{+2}(CO)$_2$.

The comparison of calculated and experiments bands for various observed Pd and Pt complexes is summarized in Table 3.

Structures	u$_{calc}$(L)^a	u$_{exp}$
Pd$^+$(NO)	1804	1805
Pd^{2+}(CO)	2114	2110
Pd^{2+}(CO)$_2$	2172;2138	2214; 2193
Pd^{2+}(NO)	1843	1865
Pd^{2+}(CO)(NO)	2146/1830	2150/1800
Pd^{2+}(CO)(OH)^e	2121	2133-2147
Pd^{2+}(CO)(C$_2$H$_4$)	2140	2140
Pd^{2+}(NO)(C$_2$H$_4$)	1807	1774
Pt^{2+}(CO) (in 6-MR)	2108	2118
Pt^{2+}(CO)_a (in 8-MR)	2138	2133
Pt^{2+}(CO)_b (in 8-MR)	2134	2133
Pt^{2+}(CO)$_2$_a (in 8-MR)	2156;2108	2186;2153
Pt^{2+}(CO)$_2$_b (in 8-MR)	2179;2135	2186;2153

Table 3. Comparison between calculated (u$_{calc}$) and experimental (u$_{exp}$) CO and NO Frequencies (in cm^{-1}) in the complexes of Pd$^+$, Pd^{2+} and Pt^{2+} cations located in the zeolite.

^{a} the C-O vibrational frequencies are shifted by +35 cm^{-1} since the calculated C-O vibrational frequency for a CO molecule in gas phase 2108 cm^{-1} is lower by 35 cm^{-1} with respect to the experimental value, 2143 cm^{-1}.

In the case of Ag/SSZ-13, non-classical silver [Ag(CO)]$^{+1}$ with a C-O stretch at 2186 cm^{-1}, and, at higher CO pressures(>1 Torr), non-classical [Ag(CO)$_2$]$^{+1}$ species with a C-O stretch at 2177 cm^{-1} is also formed in SSZ-13 at room temperature (Fig. 4).[25,26,45] This is in excellent agreement with the work by the Strauss group[25,26,45]. Indeed, they found that the Ag^{+1} salt of the weekly coordinating anion [Nb(OTeF$_5$)$_6$]$^-$ can form Ag(CO)$^+$ and Ag(CO)$_2$$^+$ with CO signatures of 2208 and 2198 cm^{-1}, respectively, in good agreement with CO split between mono- and dicarbonyl Ag complexes in SSZ-13. Only under pressures above 13 atmospheres could the authors observe the formation of [Ag(CO)$_3$]$^{+1}$. Similarly to Pt and Pd, the CO stretches with Ag in the confined microvoids of SSZ-13 are downshifted.

These complexes do not decompose in the presence of significant amounts of water signifying a general trend for SSZ-13 to stabilize such complexes selectively with remarkable stability in the presence of water (Fig. 5).
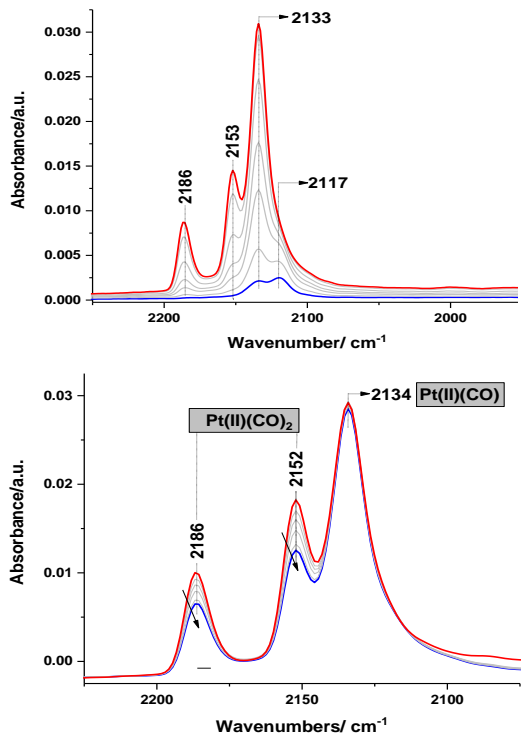
Figure 3. FTIR spectra collected on 1wt% Pt(II)/SSZ-13 (Si/Al=6) at P_{CO}=5 Torr CO pressure (a) and after evacuation (b) at 298 K
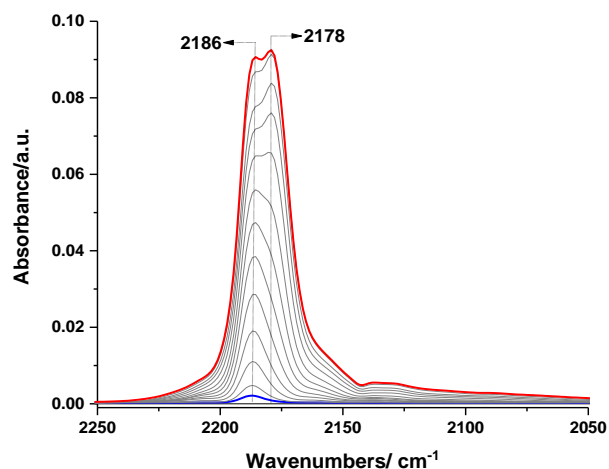

Figure 4. FTIR spectra recorded from 3 wt% Ag/SSZ-13 (Si/Al=6) during step-wise CO adsorption ($P_{CO, max.}$=10 Torr).
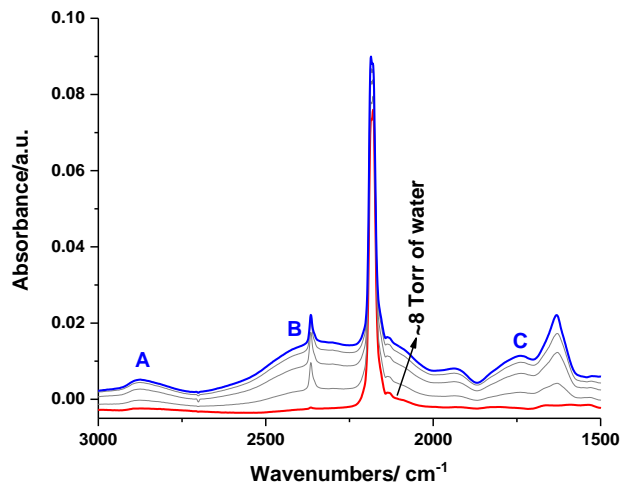

Figure 5. A series of FTIR spectra recorded during the step-wise H_2O exposure ($P_{H2O, max.}$ =~8 Torr) of Ag-CO/SSZ-13 (Si/Al=6) sample: Ag(CO) and Ag(CO)$_2$ are stable in the presence of water (while the typical ABC structure of water in zeolite appears upon water adsorption) at 298 K.[59]

The non-classical nature of the $Pd^{+2}(CO)_2$ cation also explains why its vibrational frequencies are similar for a range of zeolites. The unique 0.85 nm in diameter cavity in SSZ-13 seems to be a great stabilizer for such species. Its additional charge transfer character is also evident based on the intense pink-purple color of the complex upon CO adsorption (Fig S5). Previous studies claimed the formation of Pd(IV) cation on various solid supports and zeolites based on (1) the indirect evidence from stoichiometry from XRD refinement[27] (2) DFT-modeling[46] and (3) the presence of the high binding energy feature (relative to PdO with BE of Pd 3d$_{5/2}$ at 336.5-337.0 eV) in the Pd 3d XPS spectra[24,28,29,47,48]. Interestingly, in some works a feature at 337.7-338.0 eV on ceria supports, for example,[49,50,51] was attributed to Pd(IV) ions or PdO$_2$. Therefore, in order to clarify this issue and provide complementary evidence to the FTIR-based conclusions, we performed quasi *in-situ* XPS (Figs. S18-S26) and high-resolution XPS measurements (Figs. S25, S26) on the samples with 0.1 and 1 wt % Pd on SSZ-13 (Si/Al = 6). It is very important to note that for both 0.1 wt% and 1 wt% Pd/SSZ-13 Si/Al~6 samples the two lower-lying BE (binding energy) peaks of Pd 3d$_{3/2}$ and 3d$_{5/2}$, belonging to one species, selectively disappear after dehydration and form only two high-lying BE Pd 3d$_{3/2}$ and 3d$_{5/2}$ bands belonging to the other species (Figs. S25 and S26). For both Pd loadings, the Pd 3d$_{5/2}$ feature was shifted by about 2.7 eV compared to typical PdO and over 2.3 eV for Pd^{+2} XPS features observed for typical Pd hydrated or tetramine compounds. At first glance, this seems to indicate a significantly different oxidation state of Pd compared to typical Pd^{+2}. Thus, we decided to explore XPS of 0.1 wt% and 1 wt% Pd/SSZ-13 (Si/Al=6) in greater details (Tables S3,S4, Figs. S16-S24). Both feature atomically dispersed Pd as evidenced by previous HAADF-STEM, EXAFS, XRD, FTIR and DFT data.[8-10] We also note that upon dehydration either in He or O_2, the color of the sample changes from light yellow to light pink (Fig. S3). This is due to Pd interaction with water vapor. (It is known that water can interact with Pd ions in zeolite (analogous to Cu/SSZ-13) and it actually decreases its propensity to interact with NO molecules. This is why, for example, water can inhibit the performance of such materials in PNA applications in the presence of just NO.[9]) These visual changes for Pd/SSZ-13 happen at the same

temperature (~220°C) both in dry He or O_2. Upon cooling, the pink color is preserved in the absence of moisture – as soon as air/moisture contact takes place, the yellowish color resumes. High-resolution XPS shows two resolved Pd $3d_{5/2}$ peaks both for 1 and 0.1 wt% Pd samples (in the presence of moisture in the air). Their corresponding binding energies are 337.3 and 339.6 eV. The low-lying peak is near where Pd^{+2} hydrated cations typically show up and higher than highly-dispersed PdO.[29] The high-lying peak (2.3 eV higher) could potentially be attributed to Pd in a higher oxidation state. The peaks demonstrate reproducible behavior upon heating: more specifically, the low energy peak disappears and completely transforms into the high-energy peak for both 0.1 and 1 wt% Pd.

This could indicate two things: the transformation of Pd^{+2} into Pd ions with a higher oxidation state, or the removal of water coordinated to some of the Pd cations and subsequent transformation to Pd^{+2} sites with unusually high binding energy (BE). In the case of Rh prepared from $Rh(CO)_2(Acac)$ and anchored as $Rh(CO)_2$ classical fragments strongly bound to the HY framework, a single $Rh(I)(CO)_2$ is upshifted by 1 eV compared to the parent $Rh(CO)_2$ and about ~25 cm^{-1} in the FTIR spectra – a notably high value.[30,31] The zeolite, thus, indeed may act as a macroligand in whose cages/microchannels the complex sits. However, the 2.3 eV shift is exceptionally high. The possibility where Pd^{+2} is oxidized to Pd(IV) can only be envisioned via the formation of $(O_{zeolite})_2$-Pd(IV)=O (Table S1) with an unprecedented Pd=O bond (since it is impossible to have 4 Al atoms in the realistic vicinity of Pd(IV) or 3 Al atoms near Pd(IV)-OH). The formation of a compound with Pd(IV)=O bond is definitely a possibility, and in this case this would be the first case of a Pd complex with a Pd=O oxo bond: indeed, despite many attempts to prepare oxo Pd compounds all of them have failed so far. However, our previously published XANES data[8] for samples calcined in O_2 directly shows that the overwhelming majority of Pd remains in the +2 oxidation state due to the absence of typical features for Pd(IV).[14] Furthermore, in the case of 1 wt.% Pd, one could argue that some PdO may be visible but for 0.1 wt% Pd/SSZ-13, all Pd should be 100% atomically dispersed. Thus, the lower binding energy (BE) XPS feature belongs to either fully or, more likely, partially hydrated Pd cations in zeolite: such cations have the typical yellow color characteristic of mononuclear $[Pd^{+2}(H_2O)_4]$ or $[Pd^{+2}(NH_3)_4]$ cations. However, we do not believe they are fully hydrated Pd ions, but likely Pd^{+2} cations with 1 or potentially 2 H_2O molecules adsorbed onto them (or inserted between the framework and Pd^{+2}, which breaks up the Pd^{+2}/ 2 $^-O_{zeolite}$ ion pair). Indeed, our DFT calculations demonstrate that H_2O binding to Pd cations is favorable (Table S1). Upon heating, we observe water removal from Pd^{+2} and formation of a light pink Pd-zeolite system with isolated superelectrophilic Pd^{+2} cations: their superelectrophilic nature is evident based on the extremely high shift of the binding energy of Pd^{+2} feature by 2.3 eV to 339.6 eV compared to isolated (partially) hydrated Pd(II) ions in zeolite micropore. This process is reversible, as evidenced by the restoration of the yellow color in the presence of water vapor.

In order to understand whether unprecedented Pd(IV)=O species could indeed form upon oxidation, and whether oxidation of Pd(II) was responsible for the color change from yellow to pink the following experiment was conducted. We produced the pink sample (~ 300 mg, 1 wt% Pd/SSZ-13), purged it with helium and reacted it in the oxygen-free glove box with a minimum, amount of de-aerated H_2O in a closed vial with a septum. The sample turned yellow. To explain res-

toration of the yellow Pd(II)/SSZ-13 upon interaction with water, reduction of Pd(IV) to Pd(II) in the presence of water ought to take place via the following red-ox reaction: Pd(IV) + 2 e → Pd(II). As Pd accepts two electrons, water has to give electrons which can only occur by oxidizing H_2O: H_2O – 2e → 2H^+ + 1/2O_2. If Pd(IV) was reduced to Pd(II), it would produce 14 micromoles of O_2. However, no O_2 was produced, therefore no reduction took place. Furthermore, if oxidation of Pd(IV) were to take place by heating in the presence of oxygen, then during the sample heating in inert gas, the yellow sample containing hydrated Pd(II) ions would not turn pink (which happens in O_2 as well). Instead this transformation happens both in inert gas and in oxygen, confirming that no Pd(IV) is produced. Thus, Pd remains in +2 oxidation state and changes in the electrophilicity of Pd(II) ions upon water adsorption/desorption are responsible for the observed color variation. Therefore, we are able to quantify super electrophilicity quantitatively with XPS, revealing selective formation of super electrophilic isolated Pd(II) cations from isolated hydrated Pd(II) cations in SSZ-13 micropore. Because of the uniformity of 0.1-1 wt% Pd(II) complexes in SSZ-13 with Si/Al~6 and selective transformation of hydrated Pd(II) species into one type of super-electrophilic dehydrated Pd(II) species, we were able to fully unravel the unique state of the as-formed Pd(II) species and directly measure its super-electrophilicity which manifests itself by a very high (>2 eV) shift of the binding energy of the metal cation in the first-shell oxygen ligand environment. This measurement can be extended to other metals in zeolites in order to understand whether such exceptionally electrophilic species form in other cases, provided only 1 type of species can be selectively stabilized in a specific zeolite and metal does not change its oxidation state to a significant extent upon dehydration. However, we also showed that the spectroscopic infrared signature of superelectrophilic metal ions on solid supports (at least for Pd and Pt) is the formation of unusually stable non-classical carbonyl complexes with CO bands in the ~2,200 cm^{-1} region.

We also investigated the interaction of the non-classical $Pd^{+2}(CO)_2$ complex in the SSZ-13 zeolite with ethylene. In many catalytic applications (e.g., automotive exhaust abatement) the active centers can bind a number of adsorbates from the complex gas mixture they are exposed to. Therefore, identifying and characterizing the adsorbed species that can form in Pd/SSZ-13 in a gas mixture containing both CO and a hydrocarbon (e.g., ethylene) is of great interest. The possible formation of olefin complexes, similar to the cation of the Zeise salt, is also of fundamental interest. When the $Pd^{+2}(CO)_2$/SSZ-13 system was exposed to C_2H_4 at ambient temperature it completely lost it pink colour, suggesting formation of a new complex. (Fig S5). The series of FTIR spectra collected *in situ* during the exposure of $Pd^{+2}(CO)_2$ to ethylene show the gradual decrease in intensity of the two dicarbonyl bands (2193 and 2214 cm^{-1}), and the concomitant development of a new, intense feature centered at 2143 cm^{-1} (Fig. 6).
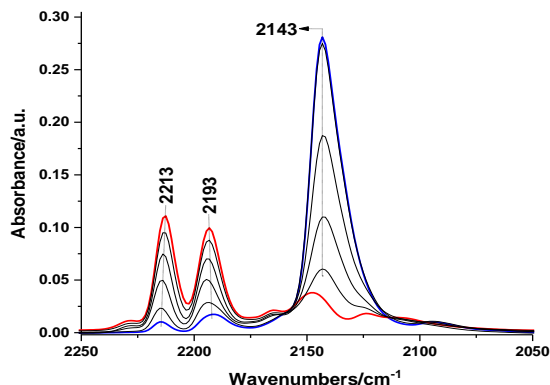
Figure 6. FTIR spectra collected during sequential ethylene adsorption on 1 wt% Pd(II)(CO)$_2$/SSZ-13 (Si/Al=6) (P$_{C2H4,}$ $_{max.}$=1.5 Torr).

These results suggest the selective formation of a Pd^{+2}(CO)(C$_2$H$_4$) complex. In fact, this is the first Pd carbonyl olefin complex observed despite prior attempts to isolate one.[32] Our DFT data are in excellent agreement with this finding, suggesting that a classical Pd(CO)(C$_2$H$_4$) (CO stretch below gas phase CO) complex formed which is anchored to the framework (Table S1). This is further corroborated by the color change from purple to white upon first pulses of ethylene (Fig S5).

The CH-stretching region shows very weak bands above 3000 cm^{-1} wavenumbers, similar to Zeise's salt C-H stretches, confirming the presence of a Pd-C$_2$H$_4$ moiety (Fig.7).
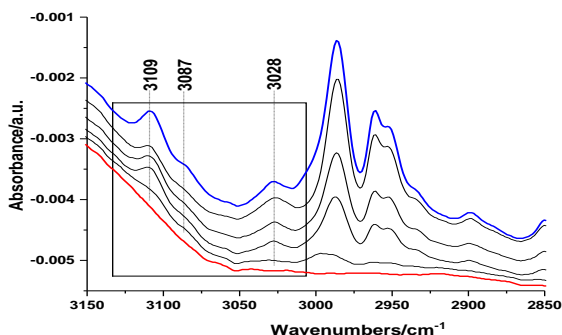
Figure 7. FTIR spectra obtained from Pd(II)(CO)$_2$/SSZ-13 (1 wt% Pd and Si/Al=6) during sequential ethylene adsorption at 298 K. (P$_{C2H4, max}$=2 Torr)

Very similar bands are observed in Rh complexes with pi-ethylene as well as Pt^{+2}-C$_2$H$_4$ and Cu-C$_2$H$_4$ pi-complexes (Fig. S27) [33,34]. This complex is stable at room temperature and does not decompose under high vacuum (Figs. S28, S29).

The classical nature of this complex is fully supported by the results of DFT calculations showing excellent agreement of the calculated C-O stretching frequencies with the experimental ones. The minor shoulder at lower C-O frequencies (2110-2120 cm^{-1}) can be attributed to the Pd^{+2}(CO) species. DFT calculations reveal that CO binding on Pd^{+2}-CO is energetically favorable by 87 kJ/mol, whereas CO binding energy on Pd(CO)(C$_2$H$_4$) increases to 151 kJ/mol (almost two times). Comparing the binding energy of ethylene in the Pd(C$_2$H$_4$) fragment without CO, (58 kJ/mole), to that in the Pd(CO)(C$_2$H$_4$) (98 kJ/mole), clearly explains the stability of this fragment. It is of great importance in the context of so-called passive hydrocarbon traps: the new concept aimed at alleviating hydrocarbon emissions during vehicle cold start. Ethylene binding to naked Pd cations is much weaker than

that in the presence of CO (CO is always present in the exhaust), which makes ethylene binding more favorable. Furthermore, ethylene desorption temperature shifts to a higher value, which is beneficial for passive HC trap materials. These results illustrate how the adsorption strength of one adsorbate can be controlled by the presence of a co-adsorbate.

Attempts to restore the original Pd^{+2}(CO)$_2$ were unsuccessful (Fig. S28) even under elevated CO pressure: we speculate that when the complex is locked in its specific framework-tethered position it is not possible for it to move back to the non-classical [Pd^{+2}(CO)$_2$]. However, one may argue that energetics could potentially be responsible for this effect: comparing energies from DFT calculations (Table S1), adsorption of two CO ligands on Pd^{+2} is exothermic in 215 kJ/mol in electronic energies, whereas adsorption of CO and C$_2$H$_4$ simultaneously is 209 kJ/mol favorable. Although, as we demonstrated earlier, DFT predictions for non-classical [Pd^{+2}(CO)$_2$] differ from the real observations, even if we assume weaker binding of CO, there should at least be some reversibility of this exchange, which is not observed. Therefore, it is indeed probable that the formation of the locked-in Pd(CO)(C$_2$H$_4$) entity bound to the framework strongly prevents its conversion back to non-classical [Pd^{+2}(CO)$_2$].

Motivated by the discovery of this mixed carbonyl/ethylene complex of Pd^{+2} in SSZ-13, we set out to investigate the possibility of the formation of other mixed-ligand ethylene complexes. To this end, we exposed a Pd^{+2}-NO complex formed via Pd^{+2}/SSZ-13 interaction with NO to ethylene and observed similar changes in the N-O stretching vibrational region as we have shown above for the carbonyl complex (Fig. 8).[35]
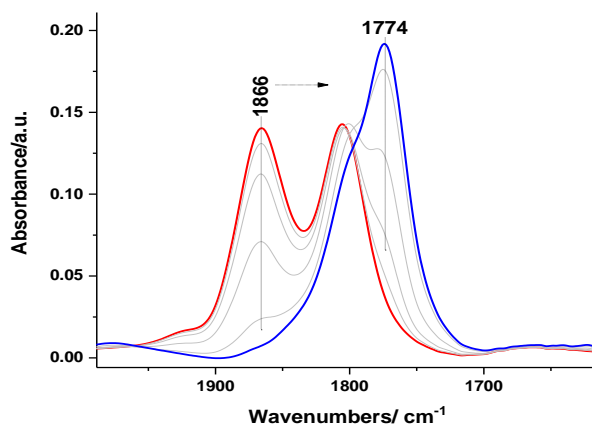

Figure 8. FTIR spectra recorded from Pd-NO/SSZ-13 (1 wt% Pd and Si/Al=6) during sequential ethylene adsorption at 298 K. (P$_{C2H4, max}$=2 Torr)

The band belonging to Pd^{+2}-NO (1865 cm^{-1}) decreased in intensity, while a new N-O stretching vibrational feature developed at 1774 cm^{-1}, indicating the transformation of Pd^{+2}(NO) to Pd^{+2}(NO)(C$_2$H$_4$) in the presence of ethylene. This is the first palladium^{+2} nitrosyl/olefin complex observed. The assignment of the new IR band was supported by the results of DFT calculations that predicted a shift of the NO stretching vibrational frequency in the Pd^{+2}-NO complex to lower wavenumbers upon its interaction with ethylene. This resulted in the formation of the Pd(NO)(C$_2$H$_4$) complex.

The exposure of the Pd(NO)(C$_2$H$_4$) to CO results in the formation of detectable Pd(CO)(C$_2$H$_4$) complex, while evacuation restores the Pd(NO) complex (Fig. S35 and S30) via eth-

ylene desorption. These results are consistent with the prediction of DFT calculations, i.e., weaker binding of C_2H_4 in the Pd(NO)(C_2H_4) complex compared with Pd(CO)(C_2H_4): C_2H_4 binding energy on nitrosyl complex is 79 kJ/mol, while it is 98 kJ/mol for the carbonyl complex (Table S1). Moreover, Fig. S35-S36 provide experimental evidence in addition to Figs. S28-S30 for the relative stabilities of the mixed NO-CO-Ethylene complexes of Pd(II) in SSZ-13 in agreement with DFT predictions (see detailed discussion in the captions of Figs. S35 and S36).

The changes in the CH-stretching region are also very interesting (Fig. 9). The low intensity of the C-H stretching band for pi-coordinated ethylene in Pd(CO)(C_2H_4) is as expected since the bands in that region have very low molar extinction coefficients. However, for Pd(NO)(C_2H_4), the C-H stretching region has a higher intensity with bands very different than the ones observed for Pd^{+2}(CO)(C_2H_4) (normalized for both sample preparations).
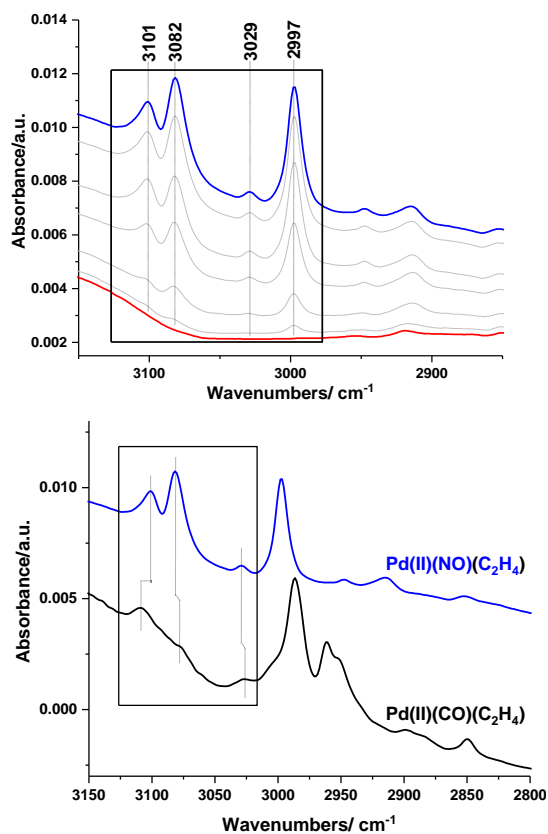
Figure 9. FTIR spectra (in the C-H stretching region) of Pd(II)(NO)/SSZ-13 (1 wt% Pd and Si/Al=6) during sequential ethylene adsorption (top) and comparison of the same region for Pd(II)(CO)$_2$ exposed to ethylene under identical conditions. ($P_{C2H4, max}$=2 Torr).

These differences seem to indicate the catalytic formation of compounds (with specific C-H stretching vibrations) during the exposure of Pd^{+2}NO to ethylene. In contrast, we did not see the development of these features on Pd(CO)(C_2H_4), indicating that the zeolite itself is not responsible for the formation (Figs 7, S31) of this compound. The developing bands during the exposure of the Pd^{+2}NO complex to ethylene did not match the characteristic features of either polyethylene or butenes. However, when a 5% butadiene/He gas mixture was introduced onto the SSZ-13, bands matching the

ones observed after ethylene exposure of the Pd^{+2}NO complex were detected (Fig. S32) (These IR features also agree well with bands reported for butadiene adsorption on various supports.[36-41])The fact that this reaction can proceed on the Pd(NO)(C_2H_4) but not on the Pd(CO)(C_2H_4) complex indicates a pronounced ligand-directing effect in this catalytic transformation of ethylene to butadiene.

Conclusions: We synthesized high loadings (1 wt%) of uniform atomically dispersed Pd(II) cations in a small-pore zeolite SSZ-13. Because of the uniformity and selective formation of the Pd(II)/2Al species for this material, we were able to unravel their unique chemistry. Previously, their spectroscopic signatures have been assigned to unselectively formed Pd(III) and Pd(IV) species; however, we here we show that in fact only [Pd(II) //2 Al] ions form selectively. We clearly prove that these Pd(II) ions are super electrophilic and quantified super electrophilicity of a metal fragment (ion) for the first time directly with the aid of high-resolution quasi in-situ XPS studies (combined with FTIR spectroscopy and DFT calculations). Because in the as-synthesized material in the presence of moisture water inserts itself between Pd(II) and basic framework oxygens (associated with framework Al T-sites), isolated hydrated Pd(II) cations form with a specific XPS signature; they dehydrate selectively forming super electrophilic Pd(II) cations (in the first-shell oxygen ligand environment, as in the case with hydrated Pd(II) cations) whose binding energy (BE) in 3d Pd XPS spectra shifts to higher BE by exceptional 2.3 eV; thus, this shift is a direct measure of super electrophilicity of a metal fragment. This XPS finding can be potentially extended to other metals in zeolites to probe whether they form super electrophilic species upon dehydration. The highly electrophilic and super electrophilic species formed in zeolites may have great importance for chemical transformation of organic molecules. The IR signatures upon CO adsorption on super electrophilic metal cations indicate formation of unusually stable non-classical carbonyl complexes with CO stretching frequencies in the 2,200 cm^{-1} region (2,214 and 2,193 cm^{-1} in the Pd(II)(CO)$_2$ case).

Thus, such Pd^{+2} ions in SSZ-13 selectively form non-classical [Pd^{+2}(CO)$_2$] complexes and Pd(I/II)-NO complexes upon CO and NO adsorption, respectively. In the presence of both CO and NO, a mixed carbonyl nitrosyl Pd^{+2}(CO)(NO) complex is formed which has been reported by us previously and which is responsible for the unique performance of Pd ions in SSZ-13 as passive NOx adsorbers. Both Pd^{+2}(CO)$_2$ and Pd^{+2}(NO) can interact with ethylene to form classical palladium carbonyl-olefin [Pd(CO)(C_2H_4)] and nitrosyl-olefin [Pd(NO)(C_2H_4)] complexes, respectively. We also show the first example of comprehensive modeling of a Pd/zeolite (and additionally Pt/zeolite) system including its interactions/activations of small molecules CO, NO, C_2H_4 – these interactions are of great importance for adsorption (e.g., passive NOx adsorbers) and catalysis.

We additionally emphasize the importance of confined nanospace (micropores) of zeolites for the formation of atomically dispersed metal ions with unusually high elecrophilicity and, as a consequence, unique physico-chemical properties. Out of them, SSZ-13 stands out due to its high hydrothermal stability and thus has a great industrial potential, for example, for low-temperature passive NOx adsorption (PNA) applications on the basis on Pd/SSZ-13 system.

Suppporting Information:

References

1. Sachtler, W. M. H. Zeolite-supported transition metal catalysts by design, *Catal. Today* **1992**, *15*, 419-429.
2. Schweizer, A.E. Noble Metal Alkaline Zeolites for Catalytic Reforming. US Patent 4992401, **1991**.
3. Klier, K., Transition-metal ions in zeolites: the perfect surface sites, *Langmuir* **1988**, *4*, 13-25.
4. Lónyi, F.; Kovács, A.; Szegedi, A.; Valyon, J., Activation of Hydrogen and Hexane over Pt,H-Mordenite Hydroisomerization Catalysts, *J. Phys. Chem. C* **2009**, *113*, 10527–10540.
5. Corma, A.; García, H., Crossing the Borders Between Homogeneous and Heterogeneous Catalysis: Developing Recoverable and Reusable Catalytic Systems, *Top. Catal.* **2008**, *48*, 8–31.
6. Haruta, M. *Chem. Rec.,* When Gold Is Not Noble: Catalysis by Nanoparticles, **2003**, 3, 75– 87.
7. Barrer, M. R. Zeolite Synthesis: An Overview, Surface Organometallic Chemistry: Molecular Approaches to Surface Catalysis, **1998**, *221-244*.
8. K. Khivantsev, N. R. Jaegers, L. Kovarik, J. C. Hanson, F. F. Tao, Y. Tang, X. Zhang, I. Z. Koleva, H. A. Aleksandrov, G. N. Vayssilov, Y. Wang, F. Gao, J. Szanyi, Achieving Atomic Dispersion of Highly Loaded Transition Metals in Small-pore Zeolite SSZ-13: a New Class of High-capacity and High-efficiency Low Temperature CO and Passive NOx Adsorbers, *Angew. Chem. Int. Ed.*, **2018,** doi:10.1002/anie.201809343.
9. Khivantsev, K.; Gao, F.; Kovarik, L.; Wang, Y.; Szanyi, J., Molecular Level Understanding of How Oxygen and Carbon Monoxide Improve NO x Storage in Palladium/SSZ-13 Passive NO x Adsorbers: The Role of NO+ and Pd +2(CO)(NO) Species, *J. Phys. Chem. C* **2018**, *122*, 10820–10827.
10. K. Khivantsev, N. R. Jaegers, L. Kovarik, S. Prodinger, M. A. Derewinski, Y. Wang, F. Gao, J. Szanyi, Palladium/Beta zeolite passive NOx adsorbers (PNA): Clarification of PNA chemistry and the effects of CO and zeolite crystallite size on PNA performance, *App. Catal. A Gen.* **2019**, *569*, 141-148.
11. A. Aylor, L, J. Lobree, J. Reimer, A. Bell, Investigations of the Dispersion of Pd in H-ZSM-5, *J. Catal.* **1997**, *172*, 453-462.
12. K. Chakarova, E. Ivanova, K. Hadjiivanov, D. Klissurski, H. Knozinger, Co-ordination chemistry of palladium cations in Pd-H-ZSM-5 as revealed by FTIR spectra of adsorbed and co-adsorbed probe molecules (CO and NO), *Phys. Chem. Chem. Phys.* **2004**, *6*, 3702–3709.
13. Moliner, M.; Gabay, J. E.; Kliewer, C. E.; Carr, R. T.; Guzman, J.; Casty, G. L.; Serno, P.; Corma, A., Reversible Transformation of Pt Nanoparticles into Single Atoms inside High-Silica Chabazite Zeolite, *J. Am. Chem. Soc.* **2016**, *138*, 15743–15750
14. S.-J. Kim, S. Lemaux, G. Demazeau, J.-Y. Kim, J.-H. Choy, X-Ray absorption spectroscopic study on LaPdO₃, *J. Mater. Chem.* **2002**, *12*, 995–1000.
15. H. A. Aleksandrov, K. M Neyman. K. Hadjiivanov, G. N. Vayssilov, Can the state of platinum species be unambiguously determined by the stretching frequency of an adsorbed CO probe molecule? *Phys. Chem. Chem. Phys.* **2016**, *18*, 22108-22121.
16. H. A. Aleksandrov, K. M. Neyman, G. N. Vayssilov, The structure and stability of reduced and oxidized mononuclear platinum species on nanostructured ceria from density functional modeling, *Phys. Chem. Chem. Phys.* **2015**, *17*, 14551-14560.
17. M. Rivallan, E. Seguin, S. Thomas, M. Lepage, N. Takagi, H. Hirata, F. Thibault-Starzyk, Platinum Sintering on H-ZSM-5 Followed by Chemometrics of CO Adsorption and 2D Pressure-Jump IR Spectroscopy of Adsorbed Species, *Angew. Chem. Int. Ed.* **2010**, *49*, 785 –789.
18. Khivantsev, K.; Vityuk, A.; Aleksandrov, H. A.; Vayssilov, G. N.; Alexeev, O. S.; Amiridis, M. D. Effect of Si/Al Ratio and Rh Precursor Used on the Synthesis of HY Zeolite-Supported Rhodium Carbonyl Hydride Complexes. *J. Phys. Chem. C* **2015**, 119, 17166– 17181.
19. G. Hwang, C. Wang, M. Bodenbinder, H. Willner, F. Aubke, The syntheses and vibrational spectra of bis(carbonyl)platinum(II) fluorosulfate and bis(carbonyl)palladium+2 fluorosulfate, *J. Fluor. Chem.* **1994**, *66*, 159-166.
20. B. von Ahsen, R. Wartchow, H. Willner, V. Jonas, F. Aubke, Bis(carbonyl)platinum+2 Derivatives: Molecular Structure of cis-Pt(CO)₂(SO₃F)₂, Complete Vibrational Analysis of cis-Pt(CO)₂Cl₂, and Attempted Synthesis of cis-Pt(CO)₂F₂, *Inorg. Chem.* **2000**, *39*, 4424-4432.
21. H. Willner, M. Bodenbinder, R. Brochler, G. Hwang, S. J. Rettig, J. Trotter, B. von Ahsen, U. Westphal, V. Jonas, W. Thiel, F. Aubke, Superelectrophilic Tetrakis(carbonyl)palladium+2 and platinum: Syntheses, Physical and Spectroscopic Properties, Their Crystal, Molecular, and Extended Structures, and Density Functional Calculations: An Experimental, Computational, and Comparative Study, *J. Am. Chem. Soc.* **2001**, *123*, 588-602. Changqing Wang/ Helge Willner/ Matthias Bodenbinder/ Raymond J. Batchelor/
22. F. W. B. Einstein, F. Aubke, Formation of cls-Bis(carbonyl)palladium+2 Fluorosulfate, cls-Pd(CO)₂(SO₃F)₂, and Its Crystal and Molecular Structure, *Inorg. Chem.* **1994**, *33*, 3521-3525.
23. G. Hwang, C. Wang, F. Aubke, H. Willner, M. Bodenbinder, The syntheses and vibrational spectra of tetrakis(carbonyl) palladium+2 and platinum+2 undecafluorodiantimonate(V), [Pd(CO)₄][Sb₂F₁₁]₂, and [Pt(CO)₄][Sb₂F₁₁]₂, *Canad. J. Chem.* **1993**, *71*, 1532-1536.
24. Zheng, Y.; Kovarik, L.; Engelhard, M. H.; Wang, Y.; Wang, Y.; Gao, F.; Szanyi, J., Low-Temperature Pd/Zeolite Passive NOx Adsorbers: Structure, Performance, and Adsorption Chemistry, *J. Phys. Chem. C* **2017**, *121*, 15793-15803.
25. P. K. Hurlburt, O. P. Anderson, S. H. Strauss, Ag(CO)B(OTeF₅)₄: the first isolable silver carbonyl, *J. Am. Chem. Soc.* **1991**, *113*, 6277–627.
26. P. K. Hurlburt, J. J. Rack, S, F. Dec, O. P. Anderson, S. H. Strauss,Bis(carbonyl)silver tetrakis(pentafluorooxotellurato)borate: the first structurally characterized M(CO)₂ complex, *Inorg. Chem.* **1993**, *32*, 373–374.
27. Lee, S. H.; Kim, Y.; Seff, K. Crystal Structure of Partially Pd²⁺-Exchanged Zeolite X Dehydrated in Oxygen at 400 °C. Formation of Linear Pd₂O₃ Clusters Proposed to Be HO-Pdᴵⱽᴼ-PdIV-OH, *J. Phys. Chem. B* **2000**, *104*, 2490– 2494.
28. O. Mihai, L. Trandafilovic, T. Wentworth, F. F. Torres, L. Olsson, The Effect of Si/Al Ratio for Pd/BEA and Pd/SSZ-13 Used as Passive NOx Adsorbers, *Top. Catal.* **2018**, *61*, 2007–2020.
29. K. S. Kim, A. F. Gossmann, N. Winograd, X-ray photoelectron spectroscopic studies of palladium oxides and the palladium-oxygen electrode, *Anal. Chem.* **1974**, *46*, 197–200.
30. Khivantsev, K.; Vityuk, A.; Aleksandrov, H. A.; Vayssilov, G. N.; Alexeev, O. S.; Amirdis, M. D., Effect of Si/Al Ratio and Rh Precursor Used on the Synthesis of HY Zeolite-Supported Rhodium Carbonyl Hydride Complexes, *J. Phys. Chem. C* **2015**, 119, 17166– 17181.
31. Khivantsev, K. Selective Synthesis and Characterization of Single-Site HY Zeolite-Supported Rhodium Complexes and Their Use as Catalysts for Ethylene Hydrogenation and Dimerization. Ph.D. Thesis, University of South Carolina, May 2015.

32. F. C. Rix, M. Brookhart, P. S. White, Mechanistic Studies of the Palladium+2-Catalyzed Copolymerization of Ethylene with Carbon Monoxide, *J. Am. Chem. Soc.* **1996**, *118*, 4746-4764.

33. G. Hubner, G. Rauhut, H. Stoll, E. Roduner, Ethyne Adsorbed on CuNaY Zeolite: FTIR Spectra and Quantum Chemical Calculations, *J. Phys. Chem. B* **2003**, *107*, 8568-8573.

34. M. J. Grogan, K. Nakamoto, Infrared Spectra and Normal Coordinate Analysis of Metal-Olefin Complexes. I. Zeise's Salt Potassium Trichloro (ethylene) platínate +2 Monohydrate, *J. Am. Chem. Soc.* **1966**, *88*, 5454-5460.

35. Khivantsev, K.; Vityuk, A.; Aleksandrov, H. A.; Vayssilov, G. N.; Blom, D.; Alexeev, O. S.; Amiridis, M. D., Synthesis, Modeling, and Catalytic Properties of HY Zeolite-Supported Rhodium Dinitrosyl Complexes, *ACS Catal.* **2017**, 7, 5965–5982.

36. S. F. Parker, C. Carias, J. Tomkinson, Vibrational spectra of buta-1,3-diene iron tricarbonyl: comparison to surface species, *Catal. Struct. React.* **2017**, *3*, 119-127.

37. Z. Wu, Z. Hao, P. Ying, C. Li, Q. Xin, An IR Study on Selective Hydrogenation of 1,3-Butadiene on Transition Metal Nitrides: 1,3-Butadiene and 1-Butene Adsorption on Mo$_2$N/γ-Al$_2$O$_3$ Catalyst, *J. Phys. Chem. B* **2000**, *104,* 12275-12281.

38. I. C. Hisatsune, Infrared spectra of 1,3-butadiene matrices containing some atomic metals, *Specrrochimica Acro.* **1984**, *40*, 391-395.

39. Z. Jing, W. Weicheng; L. Shiyang, In Situ IR Spectroscopic Study on the Hydrogenation of 1,3-Butadiene on Fresh Mo$_2$C/γ-Al$_2$O$_3$ Catalyst, *Chin. Petr. Proc. Petrochem. Tech.* **2014**, *16*, 32-37.

40. J. Silvestre-Albero, M. Borasio, G. Rupprechter, H.-J. Freund, Combined UHV and ambient pressure studies of 1,3-butadiene adsorption and reaction on Pd(111) by GC, IRAS and XPS, *Catal. Comm.* **2007**, *8*, 292–298.

41. T. V. Voskoboinikov, B. Coq, F. Fajula, R. Brown, G. McDougall, J. L. Couturier, An in situ diffuse reflectance FTIR study of the cyclodimerization of 1,3-butadiene over Cu-exchanged zeolites, *Microp. Mesop. Mat.* **1998**, *24*, 89–99.

42. Ding, K.; Gulec, A.; Johnson, A. M.; Schweitzer, N. M.; Stucky, G. D.; Marks, L. D.; Stair, P. C., Identification of active sites in CO oxidation and water-gas shift over supported Pt catalysts, *Science* **2015**, *350*, 189-192.

43. Hadjiivanov, K.I.; Vayssilov, G.N., Characterization of oxide surfaces and zeolites by carbon monoxide as an IR probe molecule, *Adv. Catal.* **2002**, *47*, 307–511.

44. G. A. Olah, D. A. Klumpp, Superelectrophilic Solvation, *Acc. Chem. Res.* **2004**, *37*, 211–220.

45. J. J. Rack, B. Moasser, J. D. Gargulak, W. L. Gladfelter, H. D. Hochheimer, S. H. Strauss, Infrared and manometric evidence for the formation of the [Ag(CO)$_3$]$^+$ complex ion at high P(CO), *J. Chem. Soc, Chem. Comm.* **1994**, 685-686.

46. A. Gannouni, F. Delbecq, M. S. Zina, P. Sautet, Oxidation of Methane to Methanol over Single Site Palladium Oxide Species on Silica: A Mechanistic view from DFT, *J. Phys. Chem. A* **2017**, *121*, 5500−5508.

47. A. Gannouni, X. Rozanska, B. Albela, M. S. Zina, F. Delbecq, L. Bonneviot, A. Ghorbel, Theoretical and experimental investigations on site occupancy for palladium oxidation states in mesoporous Al-MCM-41 materials, *J. Catal.* **2012**, *289*, 227–237.

48. S.N. Reifsnyder M. M. Otten, H. Henry Lamb, Nucleation and growth of Pd clusters in mordenite, *Catal. Tod.* **1998**, *39*, 317-328.

49. O. Pozdnyakova, D. Teschner, A. Wootsch, J. Kröhnert, B. Steinhauer, H. Sauer, L. Toth, F.C. Jentoft, A. Knop-Gericke, Z. Paál, R. Schlögl, Preferential CO oxidation in hydrogen (PROX) on ceria-supported catalysts, part II: Oxidation states and surface species on Pd/CeO2 under reaction conditions, suggested reaction mechanism, *J. Catal.* **2006**, *237*, 17-28.

50. A.L. Guimaraes, L.C. Dieguez, M. Schmal, Surface Sites of Pd/CeO$_2$/Al$_2$O$_3$ Catalysts in the Partial Oxidation of Propane, J. *Phys. Chem. B* **2003**, *107*, 4311-4319.

51. L. Meng, J.J. Lin, Z.Y. Pu, L.F. Luo, A.P. Jia, W.X. Huang, M.F. Luo, J.Q. Lu, Identification of active sites for CO and CH$_4$ oxidation over PdO/Ce$_{1−x}$Pd$_x$O$_{2−ı}$ catalysts, *Appl. Catal. B.* **2012**, *119*, 117-122.

52. J. F. Goellner, B. C. Gates, G. N. Vayssilov, N. Rösch, Structure and bonding of a site-isolated transition metal complex: Rhodium dicarbonyl in highly dealuminated zeolite Y, *J. Am. Chem. Soc.* **2000**, 122, 8056-8066.

53. K. Hadjiivanov, K. Chakarova, N. Drenchev, M. Mihaylov, Characterisation of Porous Materials by FTIR Spectroscopy of Isotopically Labelled Probe Molecules, *Curr. Phys. Chem.* **2012** 2, 151-161.

54. G. N. Vayssilov, N. Rösch, A new interpretation of the IR bands of supported Rh (I) monocarbonyl complexes, *J. Am. Chem. Soc.* **2002**, 124, 3783-3786.

55. K. Chakarova, M. Mihaylov, K. Hadjiivanov, FTIR spectroscopic study of CO adsorption on Pt–H–ZSM-5, *Microp. Mesop. Mat.* **2005**, 81, 305–312.

56. K. Chakarova, K. Hadjiivanov, G. Atanasovaa, K. Tenchev, Effect of preparation technique on the properties of platinum in-NaY zeolite: A study by FTIR spectroscopy of adsorbed CO, *J. Mol. Cat. A* **2007**, 264, 270–279.

57. Y.-S. Ryou, J. Lee, H. Lee, C. Hwan Kim, D. Heui Kim, Effect of various activation conditions on the low temperature NO adsorption performance of Pd/SSZ-13 passive NOx adsorber, *Catal. Tod.* **2019**, *320*, 175-180.

58. J. Lee, Y.-S. Ryou, S. Hwang, Y. Kim, S.-J. Cho, H. Lee, C. Hwan Kim, D. Heui Kim, Comparative study of the mobility of Pd species in SSZ-13 and ZSM-5, and its implication for catalytic activity after hydro-thermal aging as Passive NOx Adsorbers (PNAs) for cold-start applications, *Catal. Sci. Technol.* **2019**, *9*, 163-173.

59. M. F. Claydon, N. Sheppard, Nature of "A,B,C"-type infrared spectra of strongly hydrogen-bonded systems; pseudo-maxima in vibrational spectra, *J. Chem. Soc. D* **1969**, 1431-1433.

60. Khivantsev, K., Jaegers, N.R., Kovarik, L. et al. Emiss. Control Sci. Technol. (2019). https://doi.org/10.1007/s40825-019-00139-w

61. H. Kwak, R. G. Tonkyn, D. H. Kim, J. Szanyi and C. H. F. Peden, *J. Catal.,* 2010, *275*, 187.

62. Kwak, J. H.; Zhu, H.; Lee, J. H.; Peden, C. H. F.; Szanyi, J. Chem. Commun. 2012, 48, 4758– 4760.

63. Göltl, F.; Sautet, P.; Hermans, I. Angew. Chem., Int. Ed. 2015, 54, 7799– 7804.

64. N. R. Jaegers. K. Khivantsev, L. Kovarik, D. Klaus, J. Z. Hu, Y. Wang, J. Szanyi, Activation of Ethylene C-H Bonds on Uniform D8 Ir(I) and Ni(II) Cations in Zeolites: Catalytic Butadiene and Butenes Production Under Mild Conditions, *Chemrxiv* **2019** https://doi.org/10.26434/chemrxiv.8171393

65. Kwak, J. H., Lee, J. H., Burton, S. D., Lipton, A. S., Peden, C. H. and Szanyi, J. (2013), A Common Intermediate for N$_2$ Formation in Enzymes and Zeolites: Side-On Cu–Nitrosyl Complexes. Angew. Chem. Int. Ed., 52: 9985-9989.

Stabilization of super electrophilic Pd^{+2} cations in small-pore SSZ-13 zeolite

Konstantin Khivantsev[1§], Nicholas R. Jaegers[1,2§], Iskra Z. Koleva[3§], Hristiyan A. Aleksandrov[3*], Libor Kovarik[1], Mark Engelhard[1], Yong Wang[1,2], Georgi N. Vayssilov[3], and Janos Szanyi[1*]

[1]Institute for Integrated Catalysis, Pacific Northwest National Laboratory Richland, WA 99352 USA

[2]Voiland School of Chemical Engineering and Bioengineering, Washington State University, Pullman, WA 99163 USA

[3]Faculty of Chemistry and Pharmacy, University of Sofia, 1126 Sofia, Bulgaria

*corresponding authors: HAA and JSz

§ these authors contributed equally KK, NRJ, IZK

METHODS

Na-SSZ-13 with Si/Al = 6 and ion-exchanged twice with 2 M NH_4NO_3 aqueous solution at 80 °C for 3 hours yielding the ammonium forms of SSZ-13. NH_4-SSZ-13 was subsequently dried under ambient conditions and then at 80 ℃. Samples with 0.1 and 1 wt% Pd, 1 wt% Pt and 3 wt% Ag loadings were prepared by modified ion exchange (for Pd and Pt) with 10 wt% $Pd(NH_3)_4(NO_3)_2$ solution (Sigma-Aldrich 99.99%) with NH_4-SSZ-13, and platinum(II) tetraamine nitrate solution, and regular ion exchange for $AgNO_3$ (99.99%) solution with H-SSZ-13 (produced by decomposition of NH_4-SSZ-13 in air at 550 °C). More specifically, minimum amount of the Pd(II) or Pt(II) precursor solution was added to zeolite in the amount approximately equivalent to the total pore volume of the zeolite. The thick paste was mixed and stirred vigorously for 30 minutes, followed by calcination in air at 650 °C for 5 h (ramping rate 2 °C/min) in case of Pd and 350°C in case of Pt. H-forms of zeolites could be used as well with identical results: in that case, Pd and Pt tetramine salts were dissolved in the minimum amount of dilute ammonium hydroxide solution (pH=11.5), mixed with zeolite to form thick paste (mixed vigorously), followed by drying and calcination in air at 650 °C for Pd and 350 °C for Pt. In the case of Ag, 1 g of H-SSZ-13 was dispersed in water and stirred with ~20 ml of 0.1 M silver nitrate solution for 3 hours; then the sample was purified by 5 successive centrifugation-redispersion cycles and dried at 80 ℃ overnight. To avoid silver auto-reduction under high vacuum in the FTIR cell, the sample was heated to 180 °C to remove residual water from Ag/SSZ-13 as quickly as possible and then immediately cooled down prior to IR measurements.

The in situ static transmission IR experiments were conducted in a home-built cell housed in the sample compartment of a Bruker Vertex 80 spectrometer, equipped with an MCT detector and operated at 4 cm^{-1} resolution. The powder sample was pressed onto a tungsten mesh which, in turn, was mounted onto a copper heating assembly attached to a ceramic feedthrough. The sample could be resistively heated, and

the sample temperature was monitored by a thermocouple spot welded onto the top center of the W grid. The cold finger on the glass bulb containing CO was cooled with liquid nitrogen to eliminate any contamination originating from metal carbonyls, while NO was cleaned with multiple freeze–pump–thaw cycles. Prior to spectrum collection, a background with the activated (annealed, reduced or oxidized) sample in the IR beam was collected. Each spectrum reported is obtained by averaging 256 scans.

HAADF-STEM was used to probe the dispersion of Pd and Pt in prepared samples. The analysis was performed with a FEI Titan 80-300 microscope operated at 300 kV. The instrument is equipped with a CEOS GmbH double-hexapole aberration corrector for the probe-forming lens, which allows for imaging with 0.1 nm resolution in scanning transmission electron microscopy mode (STEM). The images were acquired with a high angle annular dark field (HAADF) detector with inner collection angle set to 52 mrad.

Standard NOx adsorption tests were conducted in a plug-flow reactor system with powder samples (120 mg, 60–80 mesh) loaded in a quartz tube, using a synthetic gas mixture that contained ~200 ppm of NOx or (200 ppm of NOx, 200 ppm CO, 3 vw% H_2O and 14% O_2) balanced with N_2 at a flow rate of 310 sccm (corresponding to 330,000 h^{-1}).

All the gas lines were heated to over 100 °C. Concentrations of reactants and products were measured by an online MKS MultiGas 2030 FTIR gas analyzer with a gas cell maintained at 191 °C. Two four-way valves were used for gas switching between the reactor and the bypass. Prior to storage testing at 100 °C, the sample was pretreated in 14% O_2 balanced in N_2 flow for 1 h at 550 °C and cooled to the target temperature in the same feed. The gas mixture was then switched from the reactor to the bypass, and 200 ppm of NOx was added to the mixture. Upon stabilization, the gas mixture was switched back from bypass to the reactor for storage testing for 10 min. The sample was then heated to 600 °C at a rate of 10 °C/min to record the desorption profiles of gases in the effluent.

To further disprove the possibility of formation of Pd(IV) species upon calcination in oxygen, we performed the following experiment. We heated ~ 300 mg of 1 wt% Pd/SSZ-13 in dry oxygen in the quartz reactor [the reactor has valves that allow to isolate it from ambient atmosphere upon installation/removal] at 600 °C for 3 hours, cooled it down to room temperature in dry air flow, purged the reactor with dry nitrogen. Then we moved the reactor to the moisture and oxygen-free glove box without exposure to ambient air, collected the pink powder of Pd/SSZ-13 from the reactor in a 20 ml vial with a screw-cap with a septum. We took a gas-phase sample (1ml) from that vial with a GC syringe, injected it in the GC and analyzed the gas phase to confirm absence of oxygen.

Then through the septum, we introduced a minimum amount of pure de-aerated H_2O. The sample turned yellow, characteristic of Pd(II) hydrated ions. If during the interaction with water the reduction of Pd(IV) to Pd(II) were indeed to take place, then the following red-ox reaction would occur: Pd(IV) + 2 e $\rightarrow$ Pd(II). If Pd accepts two electrons, water has to give electrons which can only occur via: H_2O – 2e $\rightarrow$ $2H^+$ + $1/2O_2$. If Pd(IV) were indeed reduced to Pd(II), it would produce 14 micromoles of O_2 during this red-ox process. In the ~20 ml vial, this amount of oxygen would be equivalent to ~0.3% of oxygen by volume. This amount (and even much smaller oxygen amount) would be easily detectable with a GC. We injected 1 ml of the gas-phase from the closed vial with a GC syringe and observed no oxygen in the gas phase. Thus, no oxygen was produced, and no Pd(IV) was formed during Pd/SSZ-13 heating in oxygen.

XAS spectra were collected at X-ray beamline 9-1 of the Argonne National Laboratory. The storage ring electron energy was 7 GeV and the ring current was in the range of 495-500 mA. Prior to these measurements, each powder sample was loaded into a cell. The XAS data were collected in the fluorescence mode. Samples were scanned at energies near the Pd K absorption edge (24,350 eV). Standards (PdO, Pd foil and $K_2[PdCl_6]$ were scanned as well. PdO and $K_2[PdCl_6]$ were mixed with BN prior to scanning). 1 wt% Pd/SSZ-13 sample in Fig. S1 was calcined in air in the XAS cell at 350 °C for 1 hour, then cooled down in the air flow and XANES recorded at room temperature.

X-ray Photoelectron Spectroscopy (XPS) experiments were performed using a Physical Electronics Quantera scanning X-ray microprobe. This system uses a focused monochromatic Al Kα X-ray (1486.7 eV) source for excitation and a spherical section analyzer. The instrument has a 32 element multichannel detection system. The 80 W X-ray beam focused to 100 μm diameter was rastered over a 1.1×0.1 mm rectangle on the sample. The X-ray beam was incident normal to the sample and the photoelectron detector was at 45° off-normal. High-energy-resolution spectra were collected using a pass-energy of 69.0 eV with a step size of 0.125 eV. Note that the samples experienced variable degrees of charging. Low-energy electrons at ~1 eV, 20 μA and low-energy Ar^+ ions were used to minimize this charging. First, the 0.1 and 1 wt% Pd samples were measured as is. The samples then were heated in 10% O_2/He for 1 h at 600 °C (ramping rate 10 °C/min), followed by cooling down in O_2/He to room temperature in a flow cell attached to the XPS system. The pretreated samples were immediately transferred into the UHV chamber without exposure to the open air for the first XPS analysis. Note that following the heating treatment, adventitious carbon, ideal for binding energy (BE) calibration, became absent. Therefore, all binding energies were referenced to a Si 2p BE of SSZ-13 of 102.7 eV.

Computational Details and Models

16

We performed periodic DFT calculations using the PW91 exchange-correlation functional with dispersion correction (PW91-D2).[1,2] Vienna *ab initio* simulation package (VASP) [3,4] was employed for these calculations. Ultrasoft pseudopotentials [5,6] were used as implemented in the VASP package. The large size of the unit cell (see below) allowed us to sample the Brillouin zone using the Γ point only [7]. A plane-wave basis was used with a cutoff energy of 400 eV.

The monoclinic unit cell of the CHA framework consists of 36 T atoms. It was optimized for the pure silicate structure with dimensions: a = b = 13.675 Å, c = 14.767 Å; $\alpha = \beta = 90^o$, $\gamma = 120^o$ [8]. Two Si atoms in the unit cell located in one six-member ring were replaced with Al. The negative charges around the Al sites were compensated by the M^{2+} ion or M^+ (M = Pd or Pt) and H^+ cations or their complexes. All atoms were allowed to relax until the force on each atom was less than 5×10^{-2} eV/Å during the geometry optimization.

The total binding energy BE of all neutral ligands (CO, NO, H_2O, and C_2H_4) is calculated as follows:

$$BE = E[ZEO/M(L1)_n(L2)_m] - E[ZEO/M] - n\times E(L1) - m\times E(L2)$$

where $ZEO/M(L1)_n(L2)_m$ (n = 1, 2 or 3) is the energy of the optimized zeolite system together with the metal (M = Pd or Pt) cation and the adsorbed molecule(s); E[ZEO/M] are the energies of the pristine zeolite system, where the framework negative charges are compansated by various cationic species considered, while E(L1) and E(L2) are the energies of the adsorbate molecule(s) in the gas phase.

The adsorption energies of certain ligand (L1 or L2) in the M (M = Pd or Pt) complexes $M(L1)_n(L2)_m$, (n=1-3, m = 0 - 2) located in the pores of CHA zeolite are calculated as follows:

$$BE_{L1} = E[ZEO/M(L1)_n(L2)_m] - E[ZEO/M(L1)_{n-1}(L2)_m] - E(L1)$$

$$BE_{L2} = E[ZEO/M(L1)_n(L2)_m] - E[ZEO/M(L1)_n(L2)_{m-1}] - E(L2)$$

in the cases where there are two types of adsorbed ligands, L_1 and L_2 corresponds to the order of the ligands in the notation of the structure. For example in $Pd^{2+}(CO)(C_2H_4)$ structure CO is first ligand (L_1) and C_2H_4 is the second one (L_2).

Consistent with these definitions, negative values of BE imply a favorable interaction.

The vibrational frequencies were calculated using a normal mode analysis where the elements of the Hessian were approximated as finite differences of gradients, displacing each atomic center by 1.5×10^{-2} Å either way along each Cartesian direction. All calculated C-O vibrational frequencies were shifted by the difference of the calculated harmonic frequency of the free CO obtained with the same computational

17

approach and the experimentally measured (anharmonic) frequency of CO in the gas phase (i.e., 2143 cm^{-1}):

$$_H(C\text{-}O)^{calc} = _{Hcalculated} - _{Hcalculated}(CO\text{-gas}) + 2143.$$

In this case, the calculated ν_{CO} frequencies are corrected for both the anharmonicity (which is 35 cm^{-1} for gas phase CO) and the systematic error of the computational method, as reported earlier [9]. Such correction cannot be applied for the N-O vibrational frequencies due to the change in the oxidation state, when NO ligands are adsorbed to the metal species.

References

[1]. J.P. Perdew, Y. Wang. Accurate and Simple Analytic Representation of the Electron-Gas Correlation Energy. *Phys. Rev. B* **1992**, *45*, 13244–13249.

[2]. S. Grimme. J. Comput. Chem. 2006, 27, 1787−1799.

[3]. G. Kresse, J. Hafner. Ab Initio Molecular-Dynamics Simulation of the Liquid-Metal-Amorphous-Semiconductor Transition in Germanium. *Phys. Rev. B* **1994**, *49*, 14251–14269.

[4]. G. Kresse, J. Furthmüller. Efficiency of Ab-Initio Total Energy Calculations for Metals and Semi-conductors Using a Plane-Wave Basis Set. *Comput. Mater. Sci.* **1996**, *6*, 15–50.

[5]. D. Vanderbilt. Soft Self-Consistent Pseudopotentials in a Generalized Eigenvalue Formalism. *Phys. Rev. B* **1990**, *41,* 7892–7895.

[6]. G. Kresse, J. Hafner. Norm-Conserving and Ultrasoft Pseudopotentials for First-Row and Transition-Elements. *J. Phys.*: *Condens. Matter* **1994**, *6,* 8245–8257.

[7]. Y. Jeanvoine, J. Angyan, G. Kresse, J. Hafner. Bronsted Acid Sites in HSAPO-34 and Chabazite: An Ab Initio Structural Study. *J. Phys. Chem. B* **1998**, *102,* 5573–5580.

[8]. Ch. Baerlocher, L.B. McCusker. Database of Zeolite Structures. http://www.iza-structure.org/data-bases/.

[9]. K. Khivantsev, N. R. Jaegers, L. Kovarik, J. C. Hanson, F. F. Tao, Y. Tang, X. Zhang, I. Z. Koleva, H. A. Aleksandrov, G. N. Vayssilov, Y. Wang, F. Gao, J. Szanyi, Achieving Atomic Dispersion of Highly Loaded Transition Metals in Small-pore Zeolite SSZ-13: a New Class of High-capacity and High-efficiency Low Temperature CO and Passive NOx Adsorbers, Angew. Chem. Int. Ed., 2018, doi:10.1002/anie.201809343.
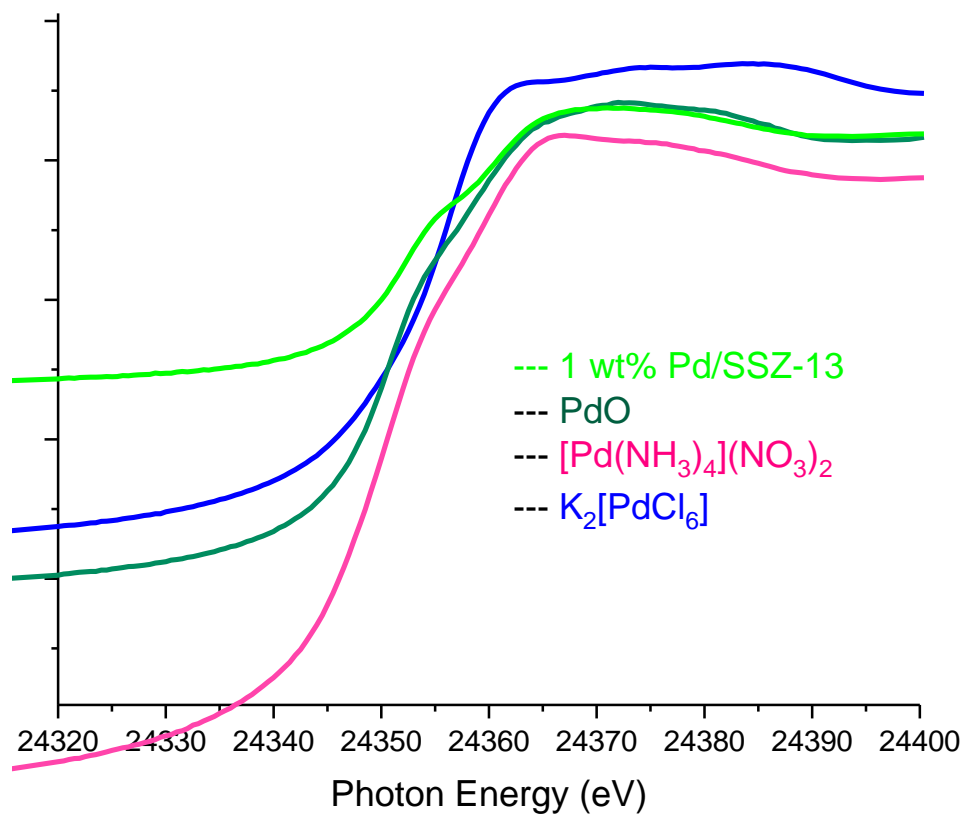
Figure S1. XANES region at the Pd K-edge of standards PdO, [Pd(NH$_3$)$_4$](NO$_3$)$_2$, K$_2$[PdCl$_6$] and comparison with air calcined 1 wt% Pd/SSZ-13.
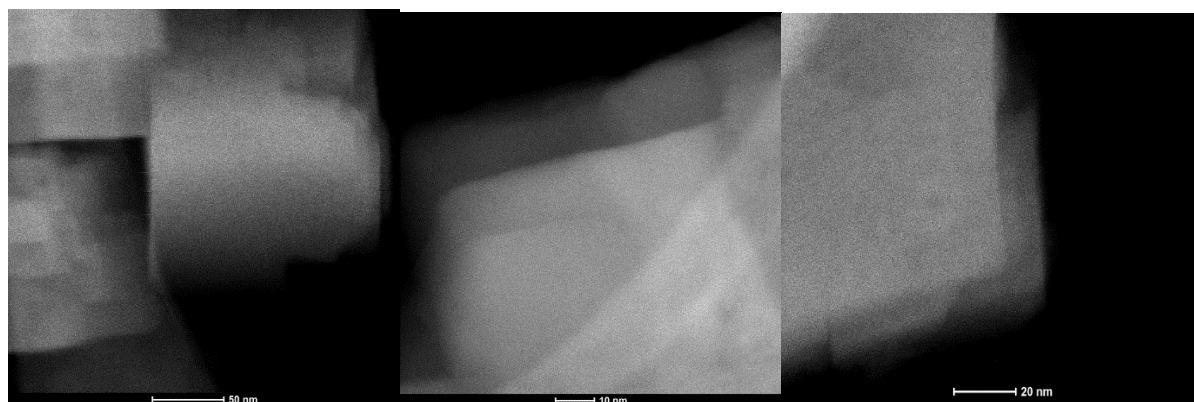
Figure S2. Cryo-HAADF-STEM images of of 1 wt% Pd/SSZ13 with Si/Al ratio 6 showing very high dispersion of Pd (no agglomeration).
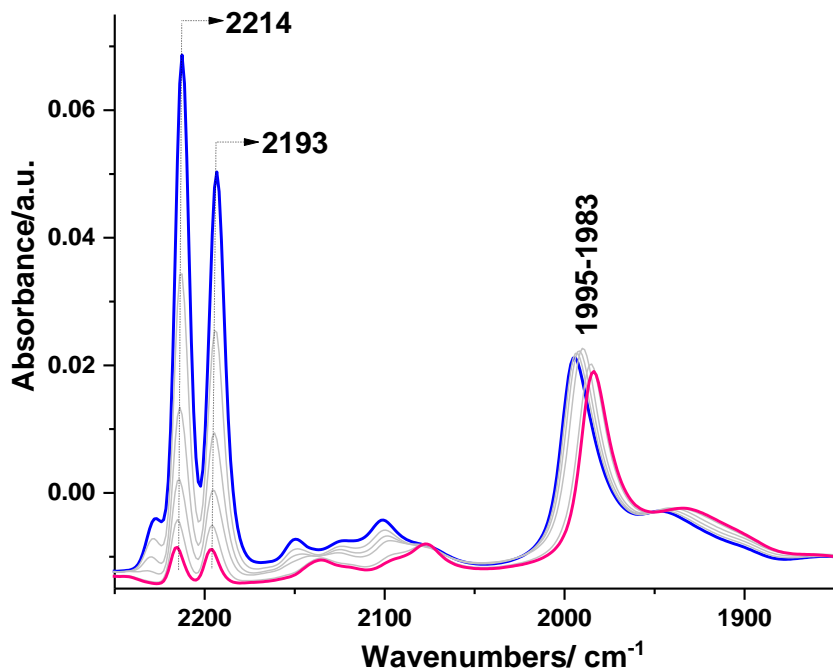
Figure S3. FTIR spectra under vacuum (from 5 Torr CO adsorbed to 0.001 Torr) on 1 wt% Pd/SSZ-13 with Si/Al=6 pre-reduced in the presence of CO (10 Torr) at 400 °C for 1 hr in the infra-red cell.
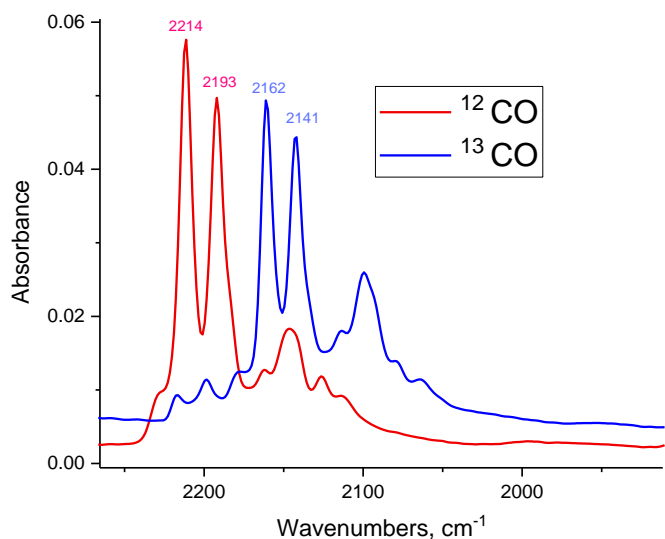
Figure S4. FTIR spectra during 5 Torr ^{13}CO adsorption on 1 wt% Pd/SSZ-13 with Si/Al=6 exposed to 5 Torr ^{12}CO prior to that.

Figure S5. Visual changes to 1 wt% Pd/SSZ-13 with Si/Al ratio 6 single-atom material: a). in the presence of moisture b). dehydrated under helium or oxygen (note that these changes are reversible; when the pink sample is stored in the glove box in the absence of moisture it retains its colour; as soon as water is added in the glovebox or the sample is taken out of the glovebox, the colour changes to yellowish) c). Pd/SSZ-13 exposed to CO d). Pd(II)(CO)$_2$/SSZ-13 exposed to a single pulse of ethylene with the formation of classical colourless (in the VIS region) Pd(II)(CO)(C$_2$H$_4$) complex.

a)   b)   c)
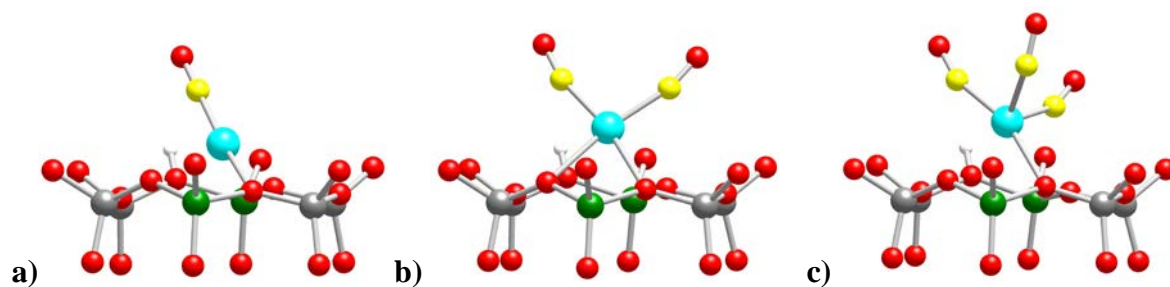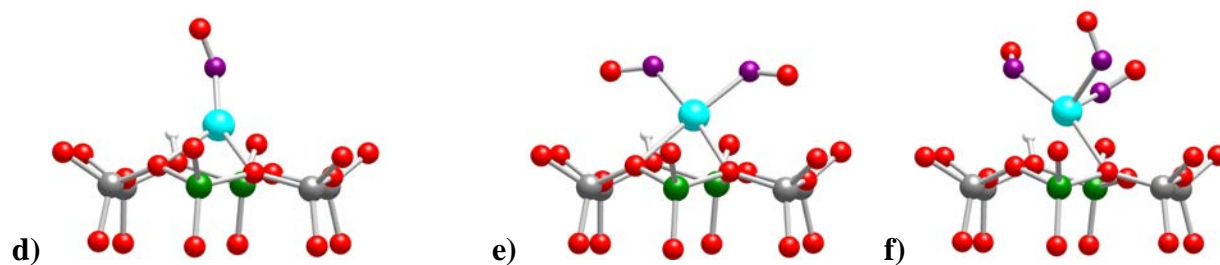
Figure S6. Optimized structures of selected Pd$^+$ complexes located in a six-membered ring of CHA: (a) Pd$^+$(CO); b) Pd$^+$(CO)$_2$, c) Pt$^+$(CO)$_3$, d) Pd$^+$(NO), e) Pd$^+$(NO)$_2$ and f) Pd$^+$(NO)$_3$. For visual clarity only local structure around the complex is shown and in some cases different views of the complexes are presented. Color coding: Si – gray; O – red; Al – green; H – white; C – yellow; N – purple; Pd – cyan.
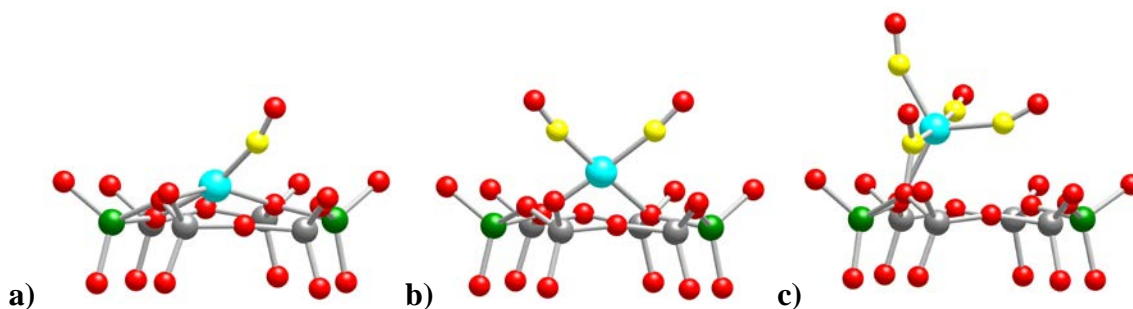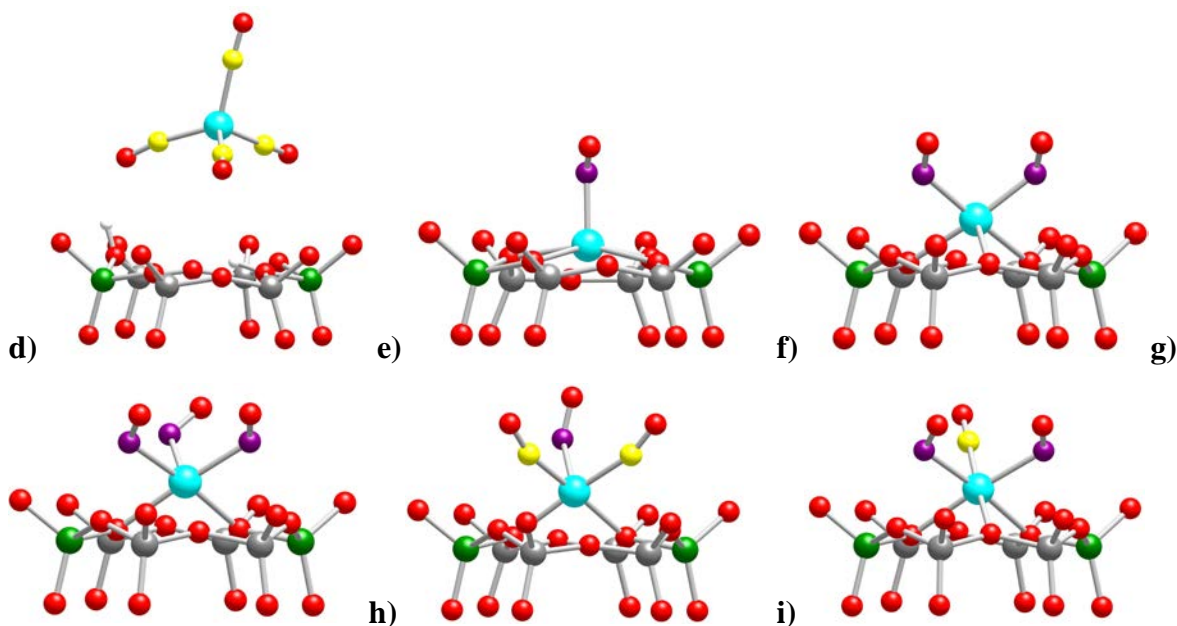
Figure S7. Optimized structures of selected Pd^{2+} complexes located in a six-membered ring of CHA: (a) $Pd^{2+}(CO)$; b) $Pd^{2+}(CO)_2$, c) $Pd^{2+}(CO)_4$ zeo, d) desorbed $Pd^0(CO)_4$ unit; e) $Pd^{2+}(NO)$, f) $Pd^{2+}(NO)_2$ and g) $Pd^{2+}(NO)_3$; mixed complexes: h) $Pd^{2+}(CO)_2(NO)$, i) $Pd^{2+}(CO)(NO)_2$. For visual clarity only local structure around the complex is shown and in some cases different views of the complexes are presented. Color coding: Si – gray; O – red; Al – green; H – white; C – yellow; N – purple; Pd – cyan.
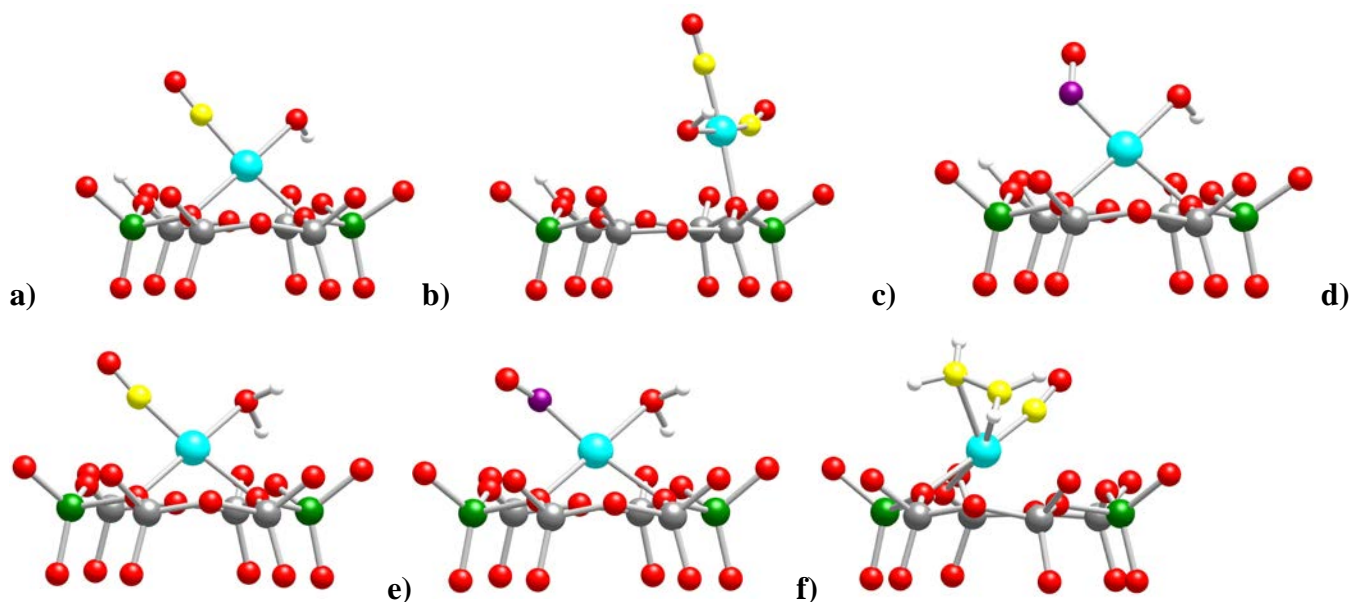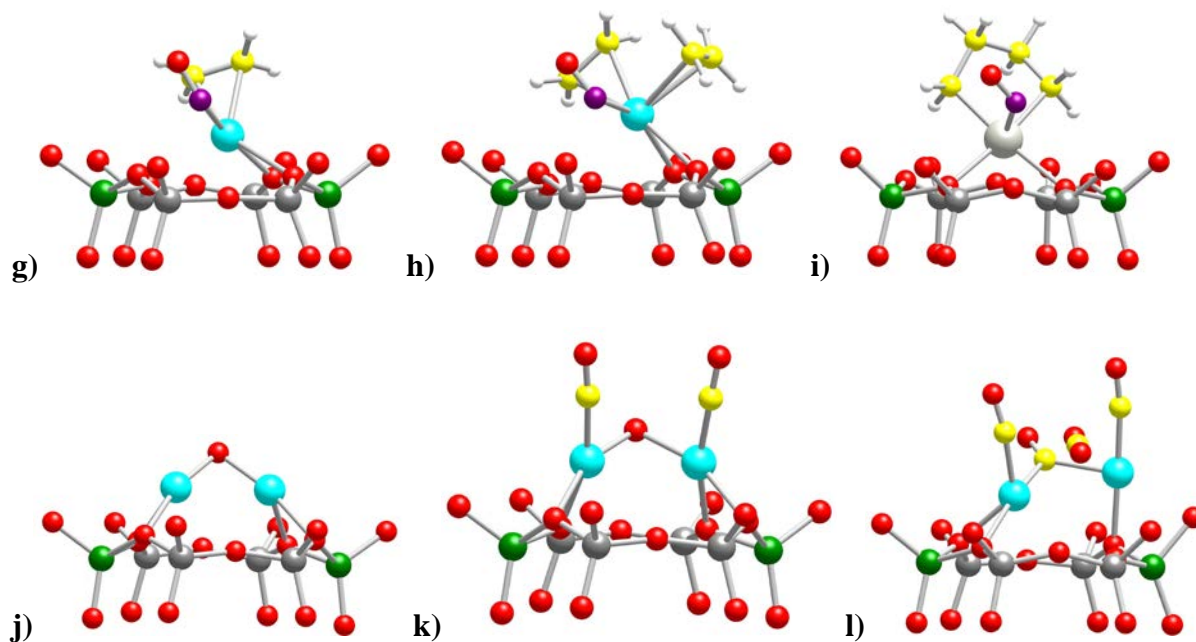
Figure S8. Optimized structures of selected Pd^{2+} complexes located in a six-membered ring of CHA: a) $Pd^{2+}(CO)(OH)$, b) $Pd^{2+}(CO)_2(OH)$, c) $Pd^{2+}(NO)(OH)$, d) $Pd^{2+}(CO)(H_2O)$, e) $Pd^{2+}(NO)(H_2O)$, f) $Pd^{2+}(CO)(C_2H_4)$, g) $Pd^{2+}(NO)(C_2H_4)$, h) $Pd^{2+}(NO)(C_2H_4)_2$ and i) $Pd^{2+}(NO)(C_4H_8)$. Models with $Pd^{2+}(O)Pd^{2+}$ dimer: j) pristine dimer, k) $Pd^{2+}(CO)(O)Pd^{2+}(CO)$, l) $Pd^{2+}(CO)_2(O)Pd^{2+}(CO)_2$ (one CO_2 is desorbed). Color coding: Si – gray; O – red; Al – green; H – white; C – yellow; N – purple; Pd – cyan.

24
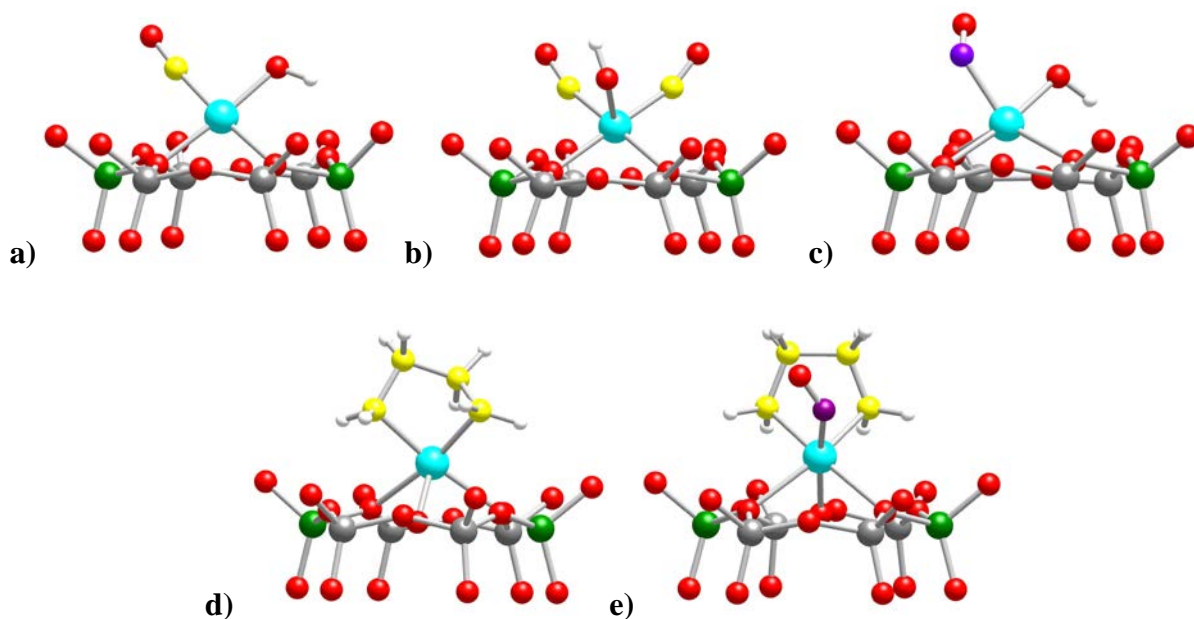
Figure S9. Optimized structures of selected Pd^{3+} and Pd^{4+} complexes located in a six-membered ring of CHA: a) $Pd^{3+}(CO)(OH)$, b) $Pd^{3+}(CO)_2(OH)$, c) $Pd^{3+}(NO)(OH)$, d) $Pd^{4+}(C_4H_8)(O)$ and e) $Pd^{4+}(NO)(C_4H_8)(O)$. Color coding: Si – gray; O – red; Al – green; H – white; C – yellow; N – purple; Pd – cyan.
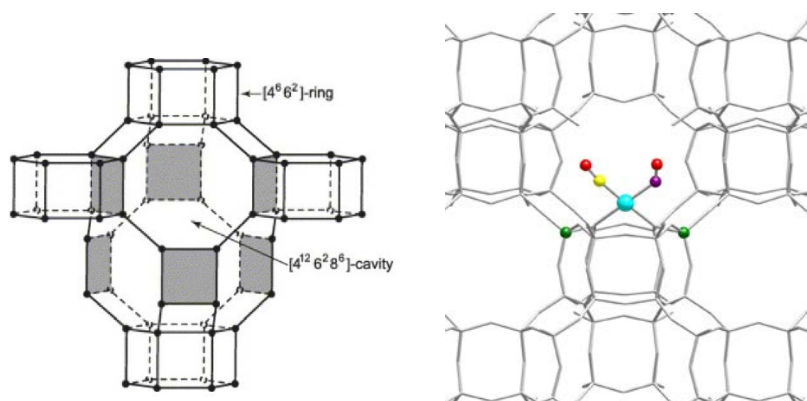
Figure S10. Crystallographic structure of SSZ-13 (chabazite) material. The diameter of the cavity is ~0.85 nm.
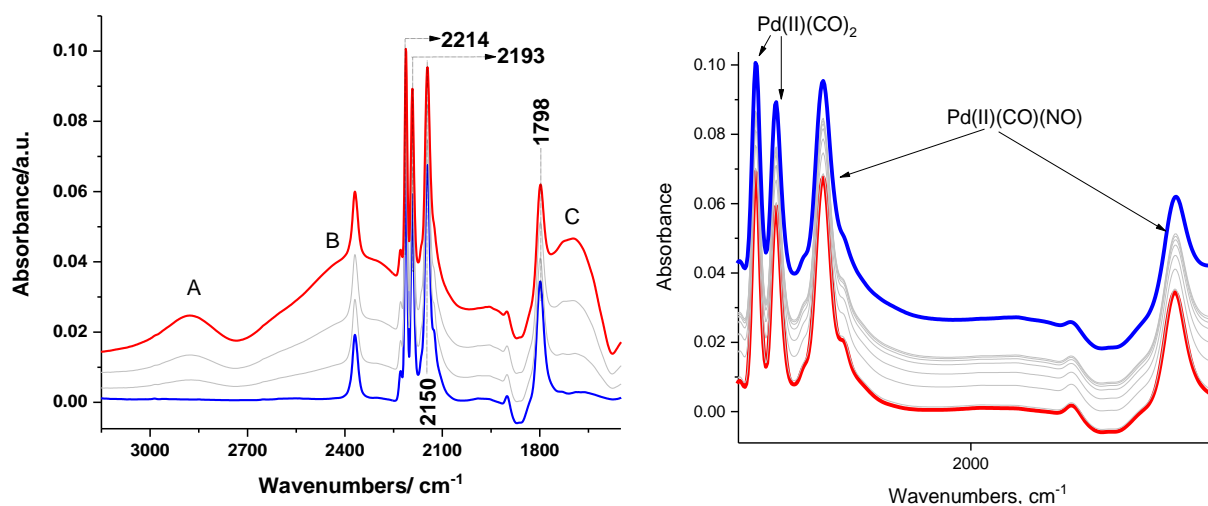
Figure S11. FTIR of sequential 6 Torr H_2O adsorption on $Pd(II)(CO)_2$ and $Pd(NO)(CO)$ in SSZ-13 (1 wt% Pd, Si/Al=6). Both complexes are stable in the presence of water (6 Torr added). ABC structure is the typical triplet feature developed upon water adsorption on zeolites in IR spectra (see, for example, Nature of "A,B,C"-type infrared spectra of strongly hydrogen-bonded systems; pseudo-maxima in vibrational spectra Claydon, M. F.; Sheppard, N., Journal of the Chemical Society [Section] D: Chemical Communications (1969).
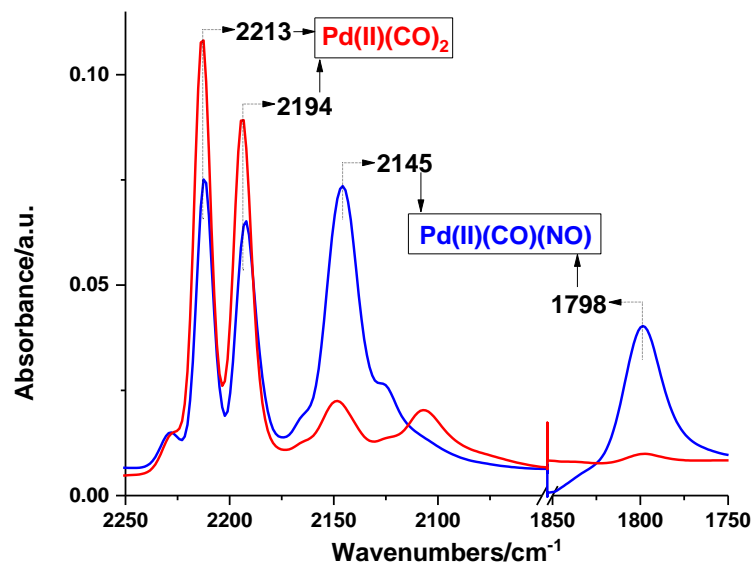
Figure S12. NO adsorption (0.2 Torr) on Pd(CO)$_2$/SSZ-13 with Si/Al=6.
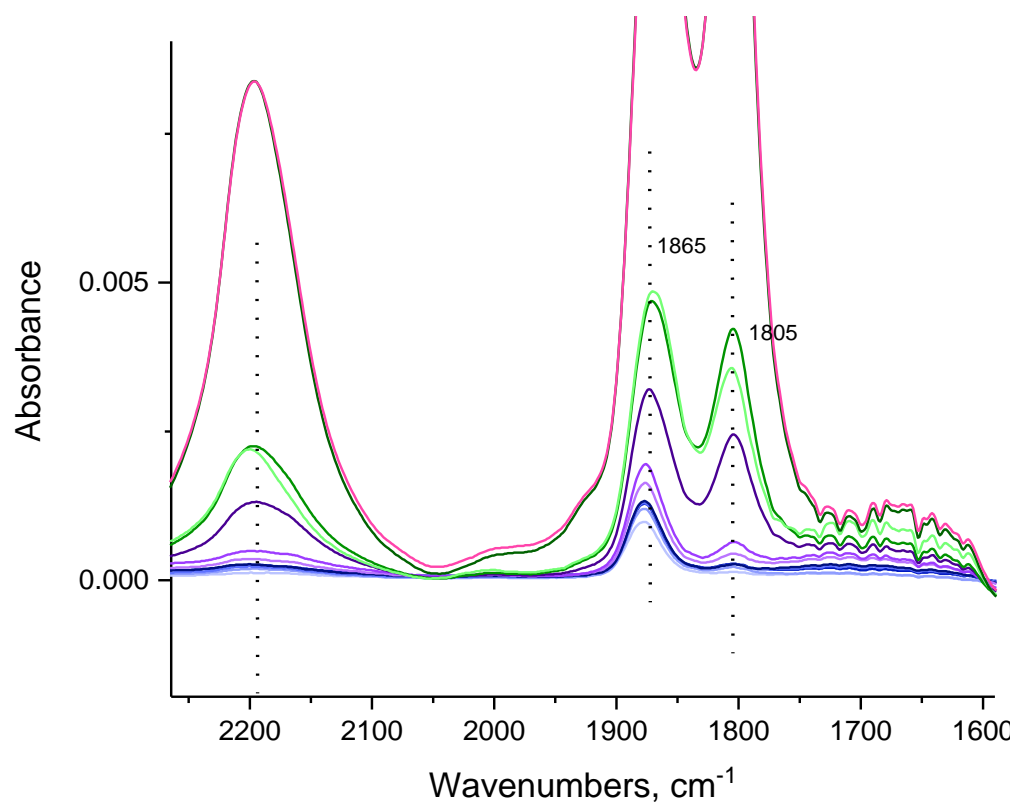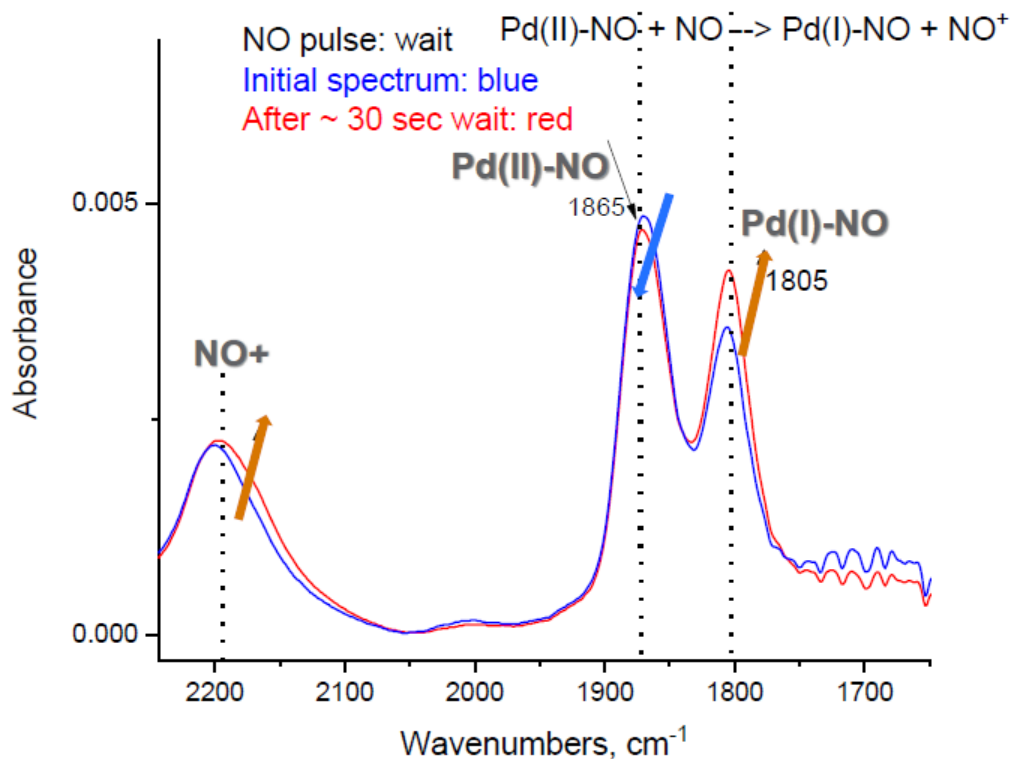
Figure S13. A) Upper figure: NO adsorption on 1 wt% Pd/SSZ-13 with Si/Al=6. B). More detailed look at NO adsorption on Pd/SSZ-13 with Si/Al=6: more specifically, after a single NO pulse the spectrum is immediately taken after pressure stabilization, and then the next spectrum is taken 30 seconds after the NO pulse. We provide the first direct experimental evidence of Pd(II) reduction by NO. NO is a free radical and addition of its unpaired electron to Pd(II) can reduce Pd(II) to Pd(I): this is exactly what we observe while looking at NO stretching frequencies; more specifically, the band pf Pd(II)-NO goes down at the expense of Pd(I)-NO that gets formed. We have previously assigned the 1,805 cm^{-1} to Pd(I)-NO on the basis of DFT calculations and common sense. Now, however, we have been able to capture this transformation in detail. The reduction of Pd(II) to Pd(I) also frees up 1 Al-O site and form nitrosyl (or alternatively nitrosonium) ion NO+ which occupies the newly available cationic position (the IR signature of this NO+ in proximity to the reduced Pd center is at about ~2,170 cm^{-1}) :

Pd(II) + NO → Pd(I)-NO + NO^{+}

This finding is the first direct extension and confirmation of our previous findings for Cu(II)/SSZ-13 system during its interaction with NO that we have reported earlier: Kwak, J. H., Lee, J. H., Burton, S. D., Lipton, A. S., Peden, C. H. and Szanyi, J. (2013), A Common Intermediate for N$_2$ Formation in Enzymes and Zeolites: Side-On Cu–Nitrosyl Complexes. Angew. Chem. Int. Ed., 52: 9985-9989. doi:10.1002/anie.201303498
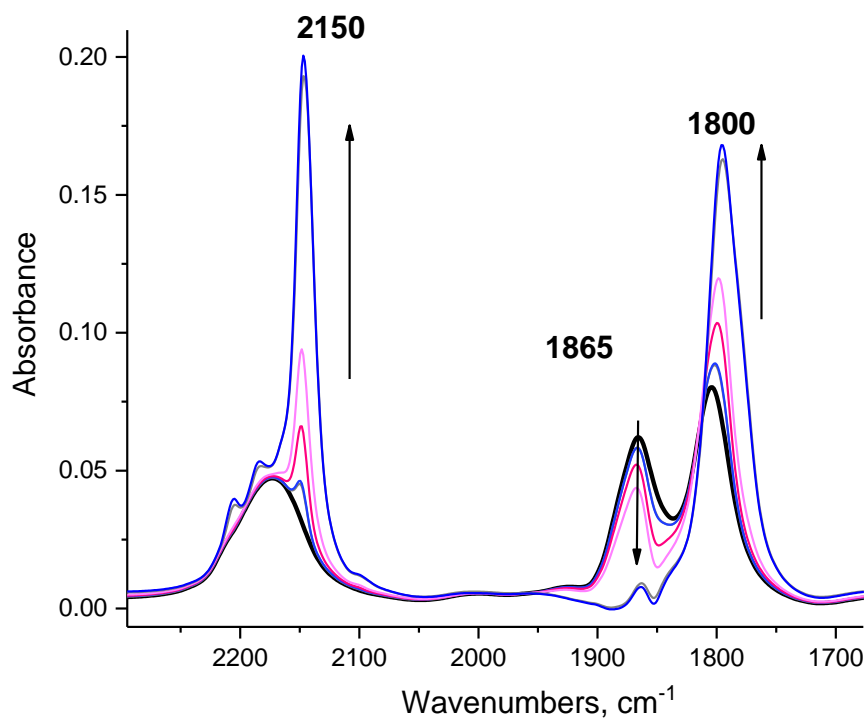
Figure S14. FTIR spectra collected during step-wise addition of 0.5 Torr CO adsorption on an NO saturated 1wt% Pd/H-SSZ-13 sample.
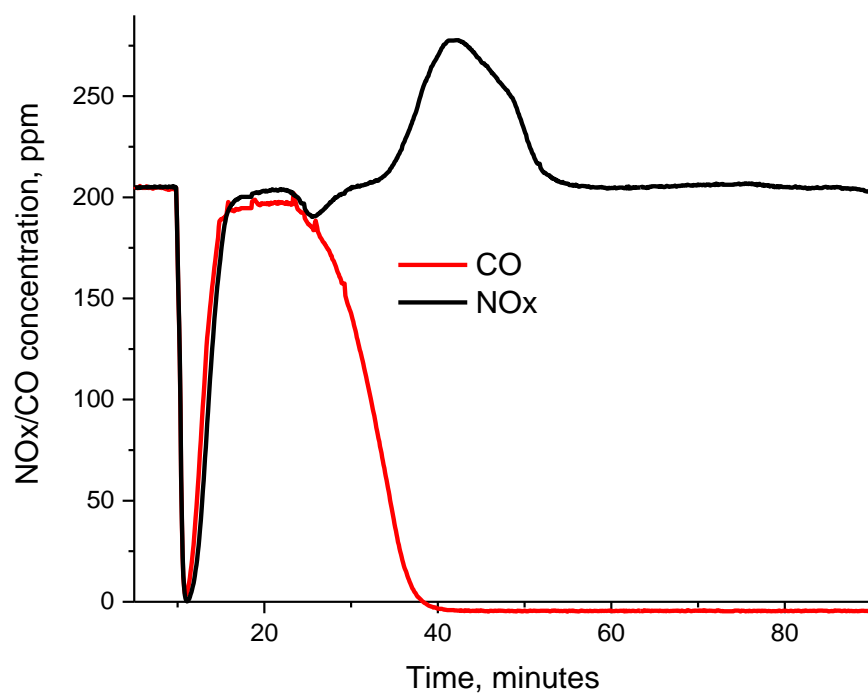

Figure S15. NOx and CO abatement performance of 1 wt% Pd SSZ-13 with Si/Al = 6. NOx adsorption at 100 °C for 10 min (after 10 min bypass) followed with TPD (10 °C/min). The feed gas mixture contains 200 ppm of NOx, 14% O_2, 3 % H_2O with with 200 ppm CO.
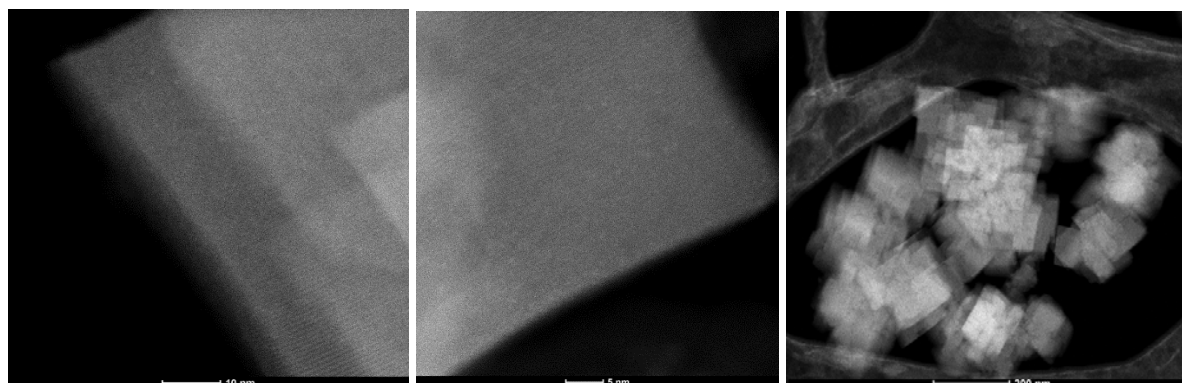
Figure S16. HAADF-STEM images of 1 wt% Pt/SSZ13 with Si/Al ratio 6.

Table S1. Binding energies of the neutral ligands (in kJ/mol), vibrational frequencies of diatomic ligands ($\upsilon(L)$ in cm^{-1}), elongation of the bond length(s) in the ligands with respect to isolated molecule in gas phase, Pd-ligand and Pd-O_{zeo} distances ($\Delta d(A-B)$, d(Pd-L), d(Pd-O_{zeo}), respectively, in pm), and number of the unpaired electrons in the systems, N_s.

Structures	BE	BE_{L1}	BE_{L2}	$\upsilon(L)^a$	$\Delta d(A-B)^b$	d(Pd-L)	d(Pd-O_{zeo})	N_s
Pd^+							220;222;225	1
$Pd^{3+}H_{zeo}$	85^c					149	215;217;224;227	1
$Pd^+(NO)$	-226			1804	0.3	181	220;231	0
$Pd^+(NO)_2$	-306	-80		1816;1739	0.1;0.8	197;223	223;235	1
$Pd^+(NO)_3$	-403	-97		1817;1740;1717	0.0;0.3;0.9	201;203;206	236;242	0
$Pd^+(CO)$	-158			2075	1.1	188	214;246;258	1
$Pd^+(CO)_2$	-252	-94		2103;2063	0.5;0.7	195;197	224;235	1
$Pd^+(CO)_3$	-273	-20		2098;2058;2055	0.6;0.7;0.7	196;201;213	230;248	1
Pd^{2+}							206;206;214;214	0
$Pd^{2+}(CO)$	-87			2114	0.4	188	206;213;214	0
$Pd^{2+}(CO)_2$	-215	-128		2172;2138	-0.2;-0.2	192;192	210;210	0
$Pd^{2+}(CO)_3$				one CO ligand desorbs				
$Pd^{2+}(CO)_{4zeo}$	-271			2178;2133;2122;1845	-0.6;-0.1;0.0;4.4^d	203;204;206;206	234	0
$Pd^0(CO)_{4\ desorbed}$				2119;2073;2068;2012	0.6;0.6;0.7;1.5	199;201;202;202		
$Pd^{2+}(NO)$	-122			1843	-1.1	193	218;219;232;233	1
$Pd^{2+}(NO)_2$	-243	-121		1879;1823	0.1;0.8	197;201	223;235	0
$Pd^{2+}(NO)_3$	-348	-104		1868;1817;1797	-1.1;-1.1;-0.8	205;207;213	229;231;254	1

29

Pd^{2+}(CO)(NO)	-200	-78	-113	2146/1830	-0.1/-1.1	193/199	213;217	1
Pd^{2+}(CO)$_2$(NO)	-252	-130	-37	2132;2111/1822	0.0;0.0/-1.0	198;198/232	219;220	1
Pd^{2+}(CO)(NO)$_2$	-319	-50	-232	2148/1852;1808	-0.3/-1.2;-1.1	199/215;215	232;238;238	0
Pd^{2+}(CO)(OH)^e		-187		2121	0.4/-0.1^g	187/198	213;219	0
Pd^{2+}(CO)$_2$(OH)		-262		2165;2125	-0.1;0.0/-0.7^g	189;197/198	215	0
Pd^{2+}(NO)(OH)^f		-177		1796	-0.1/0.1 ^{g}	189/198	219;225	1
Pd^{2+}(H$_2$O)^h	-50				0.5;7.2	206	203;215;217	0
Pd^{2+}(CO)(H$_2$O)^i	-209	-159	-122	2148	-0.1/0.7;8.0	188/209	209;210	0
Pd^{2+}(NO)(H$_2$O)^j	-203	-153	-80	1828	-1.1/0.7;6.2	191/214	212;215	1
Pd^{2+}(C$_2$H$_4$)	-58				4.7	229;229	221;221;234;235	0
Pd^{2+}(C$_4$H$_8$)	-162^k							
Pd^{2+}(CO)(C$_2$H$_4$)	-209	-151	-98	2140	0.1/6.3	188/223;224	206;221	0
Pd^{2+}(NO)(C$_2$H$_4$)	-201	-144	-79	1807	-0.7/5.8	192/224;224	216;235;254	1
Pd^{2+}(NO)(C$_2$H$_4$)$_2$	-258		-136	1817	-1.0/3.4;3.9	203/231;237;243;250	237;237	1
Pd^{2+}(NO)(C$_4$H$_8$)	-301^k		-139	1822	-1	200/214;218	227;232;251	1
Pd^{3+}(CO)(OH)		-117		2158	-0.3	192/195	210;211	1
Pd^{3+}(CO)$_2$(OH)		-160		2141;2114	0.0;0.1	194;194/217	213;213	1
Pd^{3+}(NO)(OH)		-149		1897	-2.3	203/195	212;224	0
Pd^{4+}(CO)$_2$(O)				Spontaneous formation and desorption of CO$_2$				0
Pd^{4+}(C$_4$H$_8$)(O)	-141^k					211;213	225;226;227	0
Pd^{4+}(NO)(C$_4$H$_8$)(O)	-254^k	-113		1836	-0.8	199	237;237	3
Pd^{2+}(O)Pd^{2+}							214;219/214;219	0
Pd^{2+}(CO)(O)Pd^{2+}(CO)	-321			2132/2116	0.3/0.3	188/188	214;219/214;219	0
Pd^{2+}(CO)$_2$(O)Pd^{2+}(CO)$_2$				Spontaneous formation and desorption of CO$_2$				

^{a} shifted by +35 cm^{-1} since the calculated CO in gas phase 2108 cm^{-1} is lower by 35 cm^{-1} with respect to the experimental value, 2143 cm^{-1}; the calculated frequencies of NO are not shifted. Part of the data have been reported as Supporting information in ref. [9] and here they are reported for comparison with the new data.

^{b} elongation with respect to the isolated ligand

^{c} relative energy with respect to Pd$^+$ structure

^{d} elongation of the bound CO molecule to one O from the zeolite

^{g} elongation of OH with respect to Pd^{2+}(OH)/zeo complex

Hydrogen bond between the H from OH and O from the zeolite: ^{e} 204 pm; ^{f} 203 pm.

Hydrogen bond between the H from H$_2$O and O from the zeolite: ^{h}147.8 pm; ^{i} 149.0 pm; ^{j} 154.5 pm.

^{k} With respect to two molecules ethylene
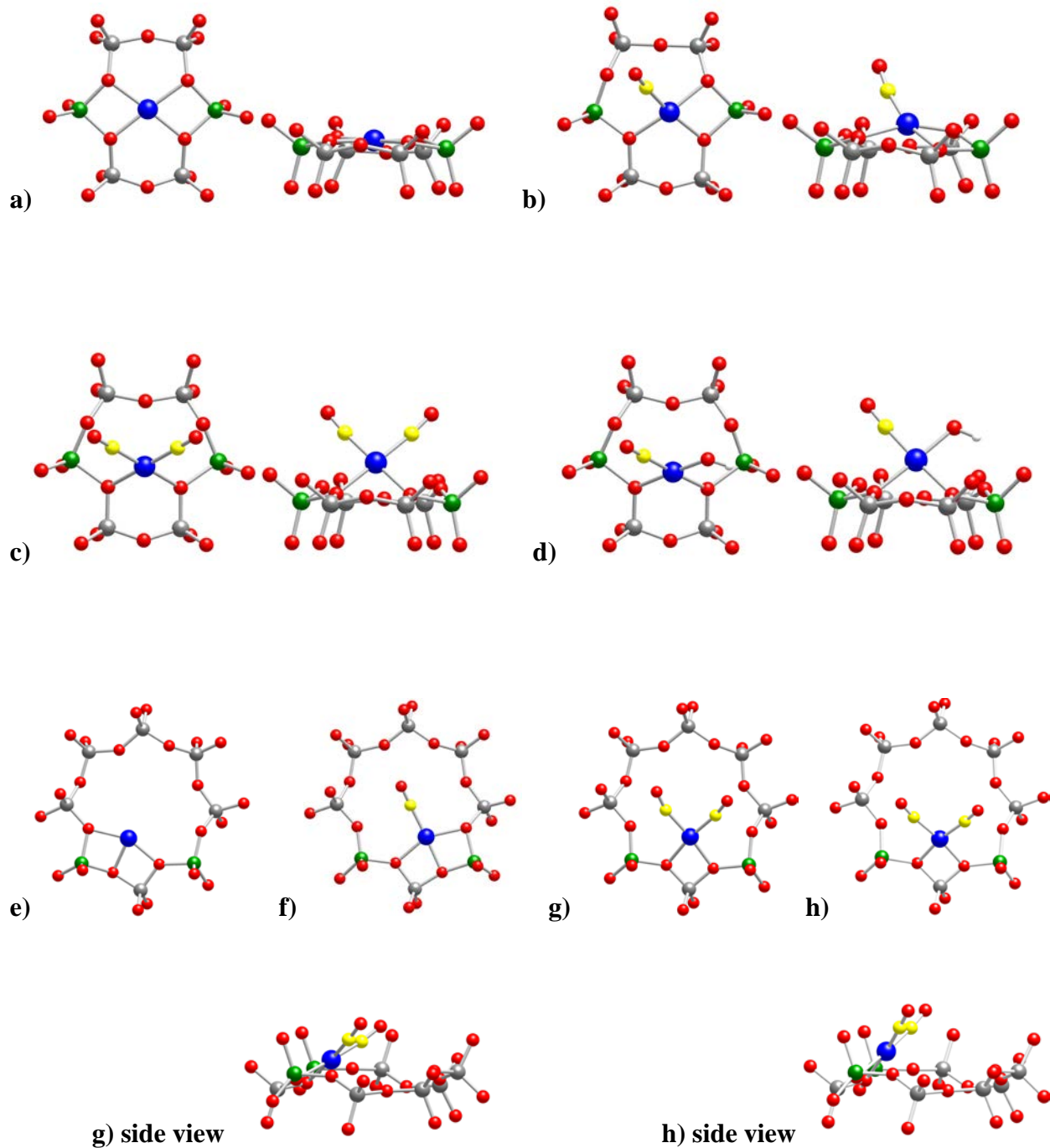
Figure S17. Optimized structures of selected Pt^{2+} complexes located in a six-membered ring of CHA: (a) Pt^{2+}; b) $Pt^{2+}(CO)$; c) $Pt^{2+}(CO)_2$ and d) $Pt^{2+}(CO)(OH)$, as well as located in eight membered ring of CHA: e) Pt^{2+}; f) $Pt^{2+}(CO)\_a$; g) $Pt^{2+}(CO)_2\_a$; h) $Pt^{2+}(CO)_2\_b$. For visual clarity only local structure around the complex is shown and in some cases different views of the complexes are presented. Color coding: Si – gray; O – red; Al – green; H – white; C – yellow; Pt – blue.

Table S2. Binding energies of all the neutral ligands (BE, in kJ/mol) and of the second adsorbed ligand (BE_{L2}, in kJ/mol), vibrational frequencies of diatomic (C-O) ligands ($x(L)$ in cm^{-1}), elongation of the C-O bond length(s) in the ligands with respect to the isolated CO molecule in gas phase, Pt-ligand distances (in pm) (Pt-L), distances between Pt cation and zeolite O centers ($Pt-O_{zeo}$) and number of the unpaired electrons in the systems, N_s.

Str.	BE	BE_{L2}	$x(L)^a$	$\Delta d(A-B)^b$	$d(Pt-L)$	$d(Pt-O_{zeo})$	N_s
Pt^{2+}						206;206;212;212	0
$Pt^{2+}(CO)$	-134		2108	0.8	185	208;211;211	0
$Pt^{2+}(CO)_2$	-318	-184	2182;2136	-0.1;0.0	189;189	209;209	0
$Pt^{2+}(OH)$					190	202;210;211	1
$Pt^{2+}(CO)(OH)$	-181		2146	0.1	188;194	209;209	1
Pt^{2+} 8 mem. ring						200;206;211	0
$Pt^{2+}(CO)$_a 8 mem. ring	-309		2138	0.5	186	202;211;212	0
$Pt^{2+}(CO)$_b 8 mem. ring	-309		2134	0.4	186	202;211;213	0
$Pt^{2+}(CO)_2$_a 8 mem. ring	-481	-173	2156;2108	0.2;0.5	190;190	206;210	0
$Pt^{2+}(CO)_2$_b 8 mem. ring	-479	-170	2179;2135	0.0;0.1	189;190	205;210	0

[a] the frequencies are shifted by +35 cm^{-1} since the calculated C-O vibrational frequency for a CO molecule in gas phase 2108 cm^{-1} is lower by 35 cm^{-1} with respect to the experimental value, 2143 cm^{-1}.

[b] elongation with respect to the isolated ligand in gas phase

Table S3. XPS data acquisition parameters.

XPS wide scan data acquisition parameters:

No	Transition	Start (eV)	End (eV)	Inc (eV)	Time/DataPt (s)	Pass Energy (eV)
1	Su1s	1350.00	0.00	-0.50	0.287	140.00

XPS narrow (high energy resolution) scan data files:

No	Transition	Start (eV)	End (eV)	Inc (eV)	Time/DataPt (s)	Pass Energy (eV)
6	O1s	541.00	523.00	-0.13	0.862	69.00
5	C1s	294.00	276.00	-0.13	1.293	69.00
4	Pd3d	354.00	328.00	-0.13	6.467	69.00
3	N1s	408.00	390.00	-0.20	2.874	112.00
2	Al2p	83.00	65.00	-0.13	0.862	69.00
1	Si2p	111.00	93.00	-0.13	0.862	69.00

Table S4. Calculated weight % of each element for 1 and 0.1 wt% Pd/SSZ-13 with Si/Al=6 "as is" and after various treatments.

```
                 --------------------------
                 Weight % Table (Calculated from XPS data)
                 --------------------------
Area Comment                                    C1s       O1s       Al2p      Si2p      Pd3d

1wt% Pd/SSZ-13 Si/Al=6   (batch 1) As is        0.87      57.49     4.32      36.80     0.51
1wt% Pd/SSZ-13 Si/Al=6   (batch 1) 600C O2      0.04      56.57     4.90      37.95     0.54
1wt% Pd/SSZ-13 Si/Al=6   (batch 1) 600C O2      0.00      55.92     4.95      38.60     0.52
1wt% Pd/SSZ-13 Si/Al=6   (batch 1) NO RT        0.05      56.27     4.75      38.32     0.61

0.1wt% Pd/SSZ-13 Si/Al=6 As is                  0.69      57.79     4.44      36.99     0.09
0.1wt% Pd/SSZ-13 Si/Al=6 600C O2                0.11      56.60     4.84      38.34     0.12
0.1wt% Pd/SSZ-13 Si/Al=6 600C NO RT             0.05      57.31     4.64      37.97     0.04
```
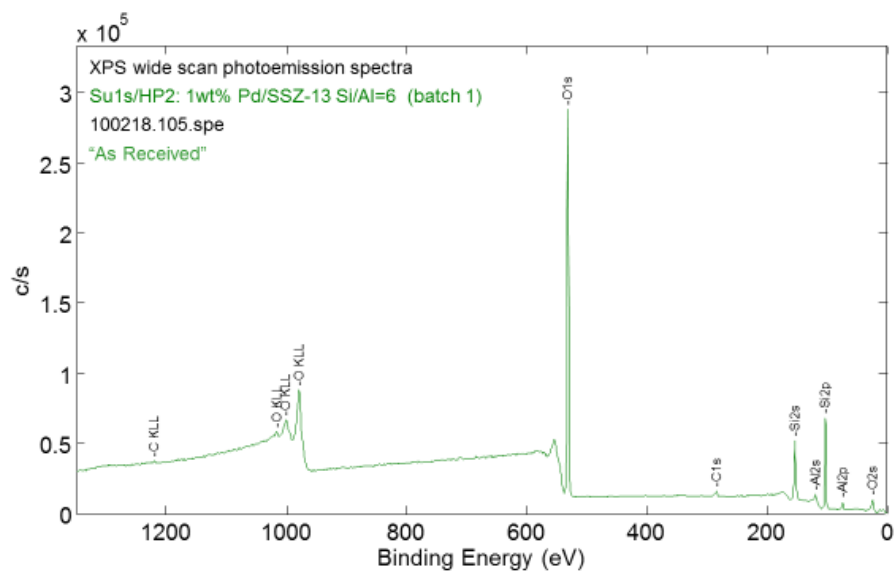
Figure S18. Wide-line XPS scan of 1 wt% Pd/SSZ-13 with Si/Al=6 as is.
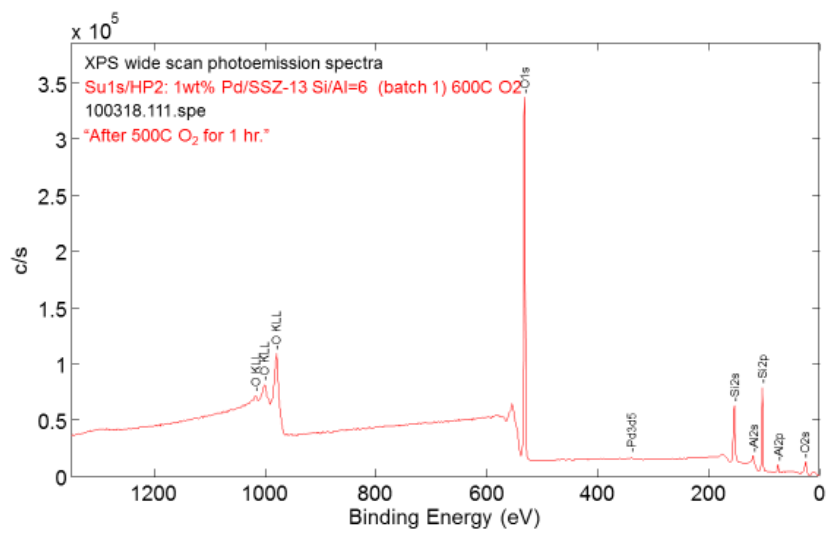
Figure S19. Wide-line XPS scan of 1 wt% Pd/SSZ-13 with Si/Al=6 calcined at 600 ℃ (taken at the first sample area).
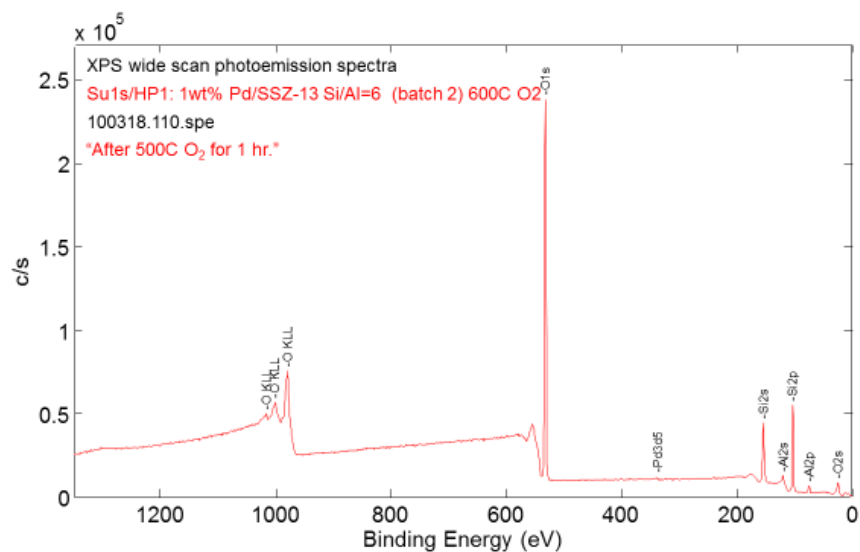

Figure S20. Wide-line XPS scan of 1 wt% Pd/SSZ-13 with Si/Al=6 calcined at 600 ℃ (taken at the 2nd sample area, different than the first one).
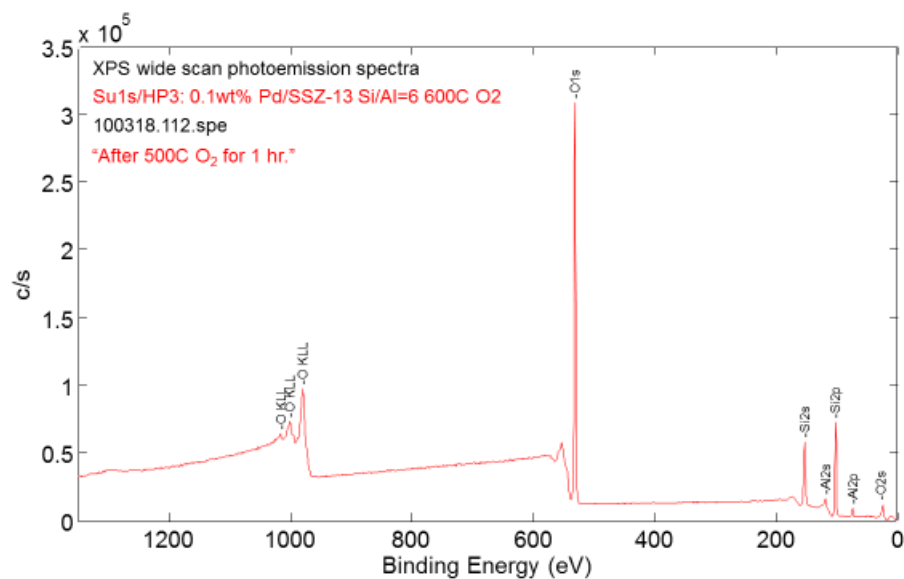

Figure S21. Wide-line XPS scan of 0.1 wt% Pd/SSZ-13 with Si/Al=6 calcined at 600 ℃.

Figure S22. High-resolution XPS scan of Si2p region for 1 wt% Pd/SSZ-13 with Si/Al=6 as is and treated under various conditions (sample was calcined at 600 ℃ in oxygen).

High energy resolution photoemission spectra
1wt% Pd/SSZ-13 Si/Al = 6 (batch 1)
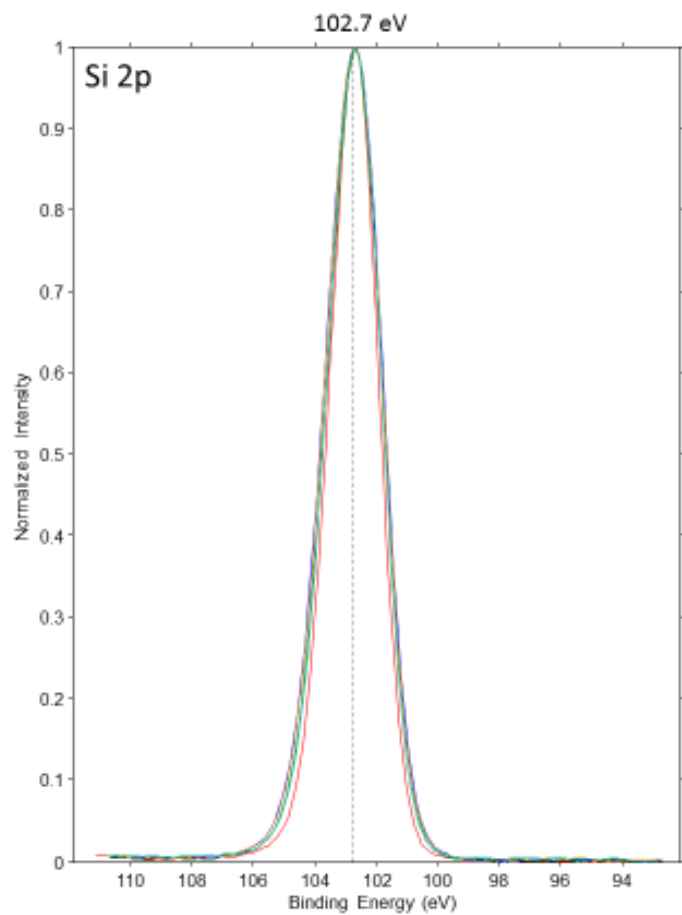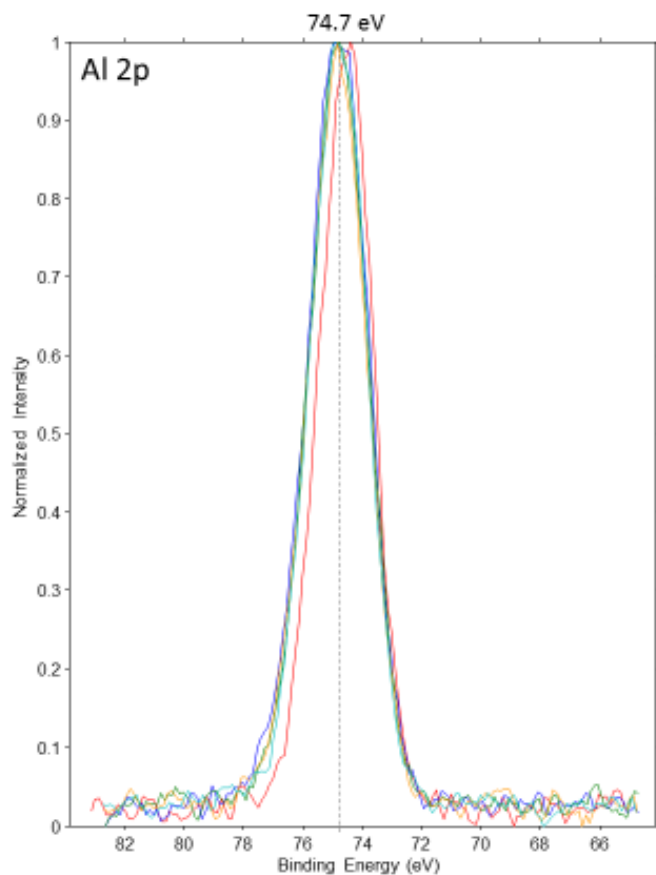
—— 100518125, HP2, "After O$_2$, 500°C 1hr." Second Ox.
—— 100318116, HP5 "After O$_2$, 500°C 1hr." Second area
—— 100318113, HP2 "After O$_2$, 500°C 1hr."
—— 100218108, HP2 "As received"

Figure S23. High-resolution XPS scan of Al2p region for 1 wt% Pd/SSZ-13 with Si/Al=6 as is and treated under various conditions (sample was calcined at 600 °C in oxygen). Importantly, we report for the first time the shift of Al BE to the left (by ~0.4 eV to higher binding energy, meaning that Al site becomes more positive) due to water leaving zeolite micropores: this confirms that water occluded in zeolite micropores under ambient conditions interacts predominantly with Al-O sites (and not O-Si sites, hence no shift in the Si BE during dehydration in Fig. S22)); thus, interaction of Al-O-H (where Al is the framework T site) with water modulates the properties of T-sites to an extent (makes them more basic) which has significant importance for chemical (organics) conversion in zeolites in the presence and absence of water. This finding complements, for example, the following data for water intraction with the zeolite obtained with state-of-the-art solid-state MAS NMR techniques: Genesis and Stability of Hydronium Ions in Zeolite Channels, Meng Wang, Nicholas R. Jaegers, Mal-Soon Lee, Chuan Wan, Jian Zhi Hu, Hui Shi, Donghai Mei, Sarah D. Burton, Donald M. Camaioni, Oliver Y. Gutiérrez, Vassiliki-Alexandra Glezakou, Roger Rousseau, Yong Wang, Johannes A. Lercher, J. Am. Chem. Soc.2019, 141, 8, 3444-3455.

Figure S24. High-resolution XPS scan of C1s region for 1 wt% Pd/SSZ-13 with Si/Al=6 as is and treated under various conditions(sample was calcined at 600 ℃ in oxygen).

Figure S25. High-resolution XPS spectra for 0.1 wt% Pd/SSZ-13 with Si/Al ratio 6 before (red) and after heating in oxygen at 600ºC (experiments performed quasi *in-situ*).

Figure S26. High-resolution XPS spectra for 1 wt% Pd/SSZ-13 with Si/Al ratio 6 before (red) and after heating in oxygen at 600°C (experiments performed quasi *in-situ*).
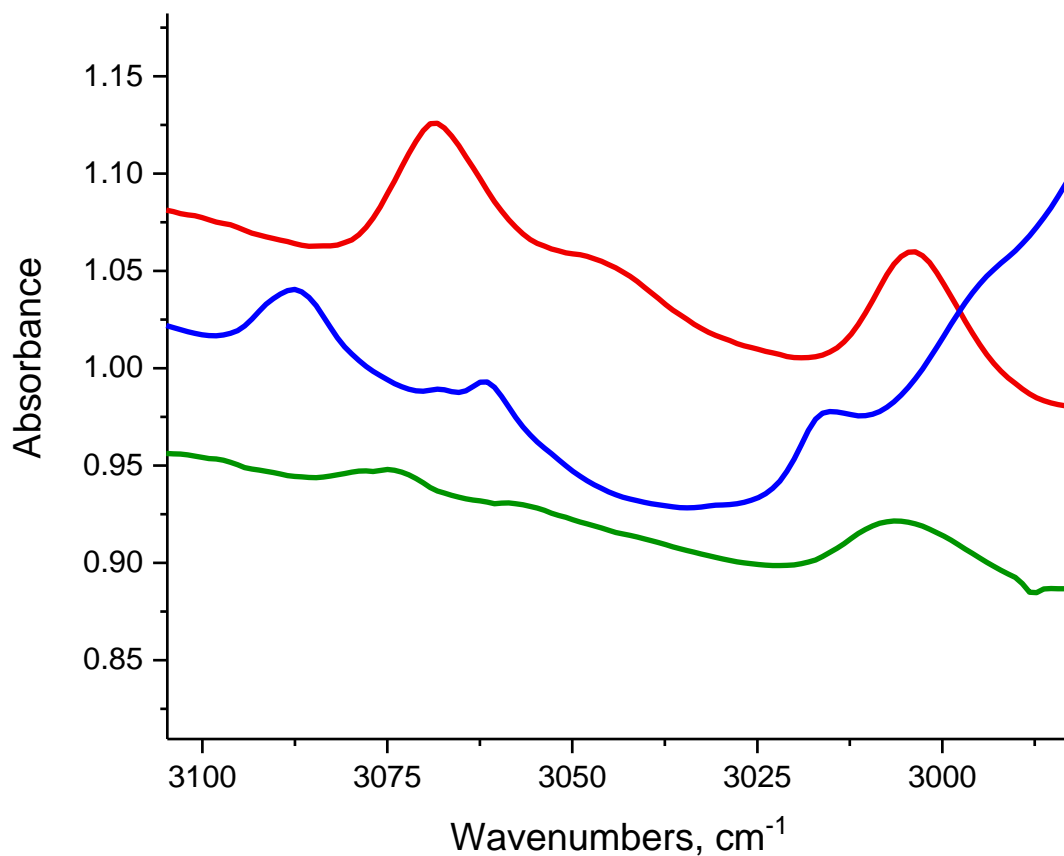
Figure S27. C-H stretching regions of Rh(C_2H_4)$_2$ on zeolite (blue line), alumina (red line) and Rh(CO)(C_2H_4)(Acac) (green line).
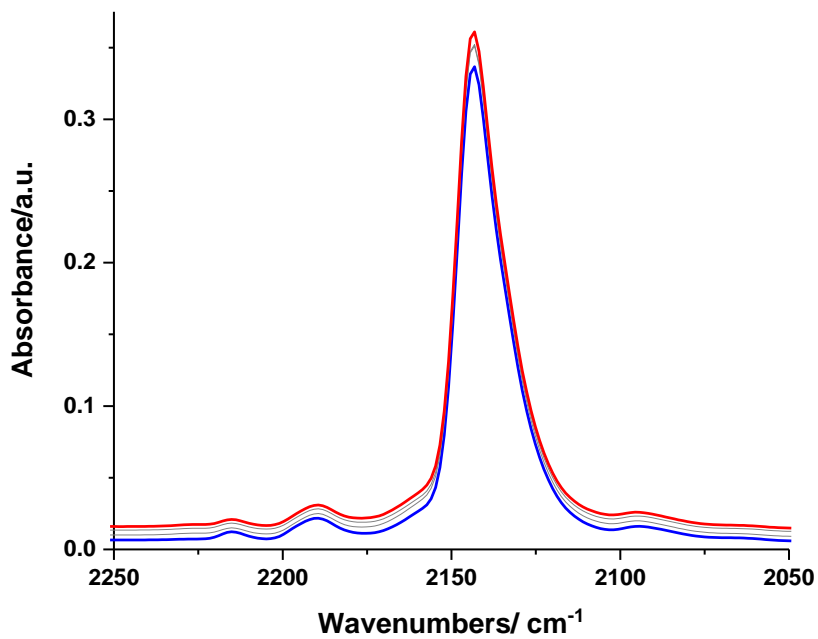
Figure S28. FTIR spectra of the CO adsorption (10 Torr) on the Pd(II)(CO)(C$_2$H$_4$)/SSZ-13 with Si/Al ratio 6.
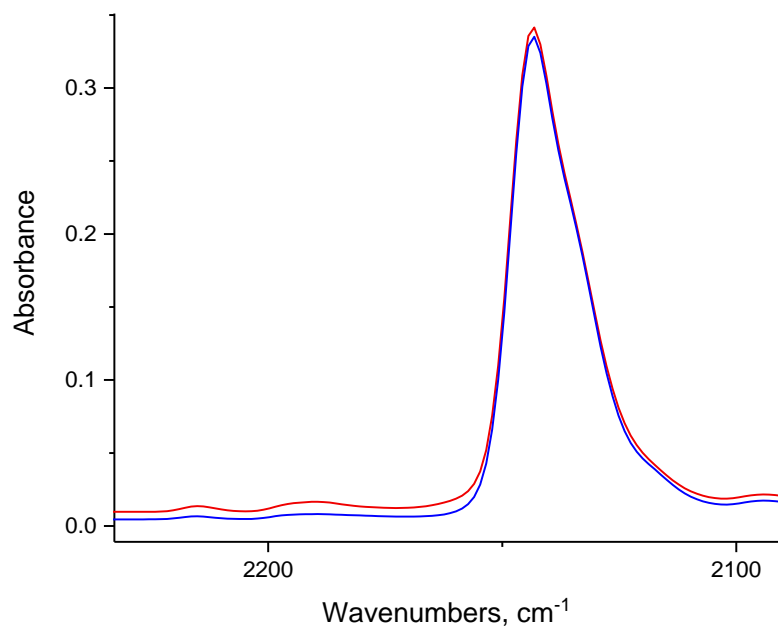
Figure S29. FTIR spectra of the high vacuum (10^{-6}-10^{-7} Torr) on the Pd(II)(CO)(C$_2$H$_4$)/SSZ-13 with Si/Al ratio 6.
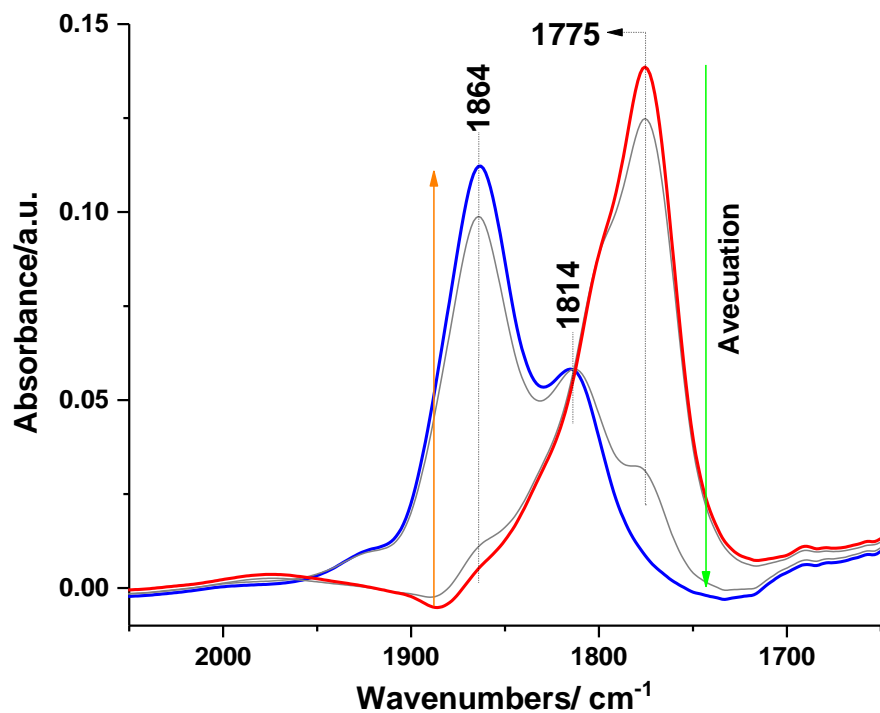
**Figure S30.** FTIR spectra of applying high vacuum on the $Pd(II)(NO)(C_2H_4)$/SSZ-13 with Si/Al ratio 6.
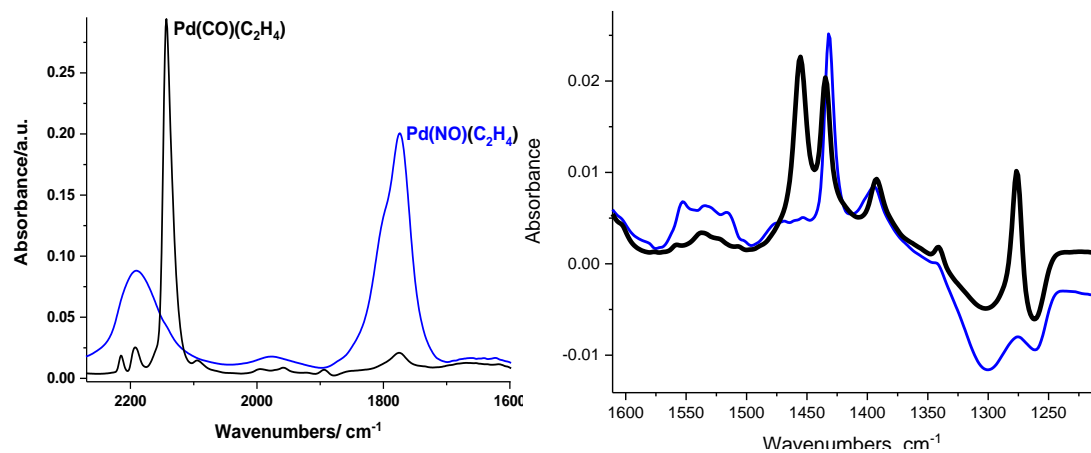
Figure S31. FTIR spectra of the comparison between $Pd(II)(CO)(C_2H_4)$ (black spectrum) and $Pd(NO)(C_2H_4)$/SSZ-13 (blue spectrum) with Si/Al ratio 6 after C_2H_4 adsorption on Pd carbonyl and nitrosyl complexes: CO/NO stretching and C=C vibrations regions are shown in addition to C-H stretching region in the main text.
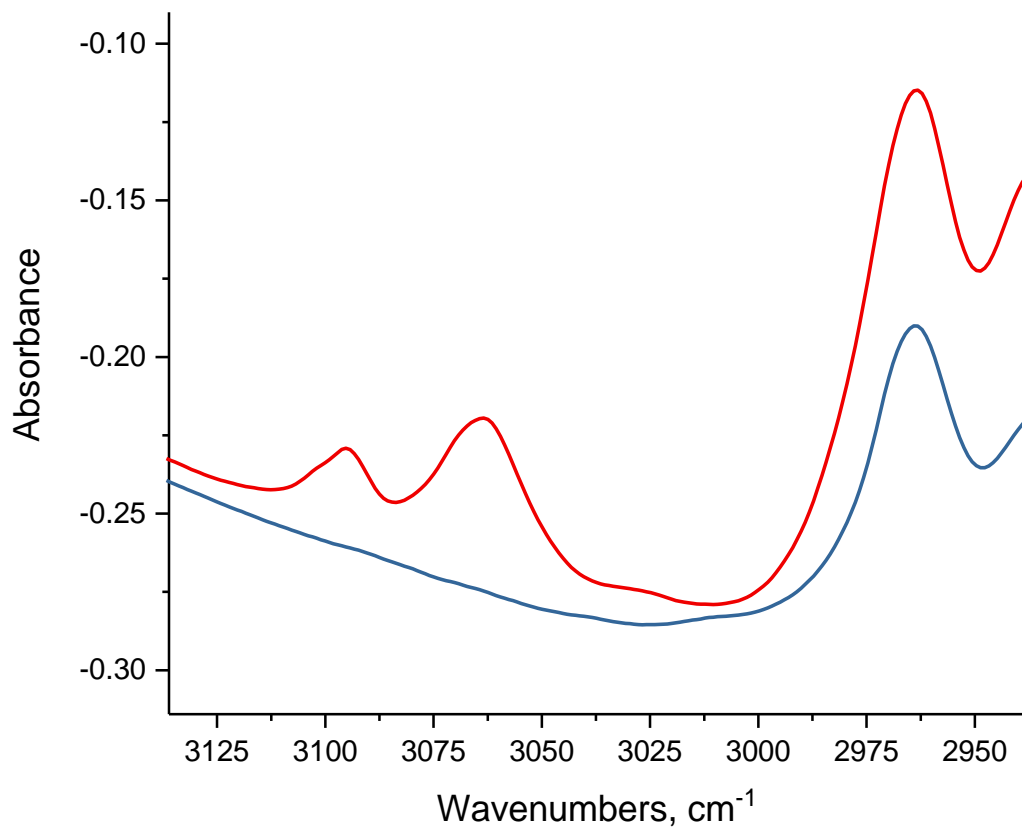
Figure S32. C-H stretching region of 5% butadiene adsorption on zeolite (blue line before adsorption, red line after butadiene-1,3 adsorption).
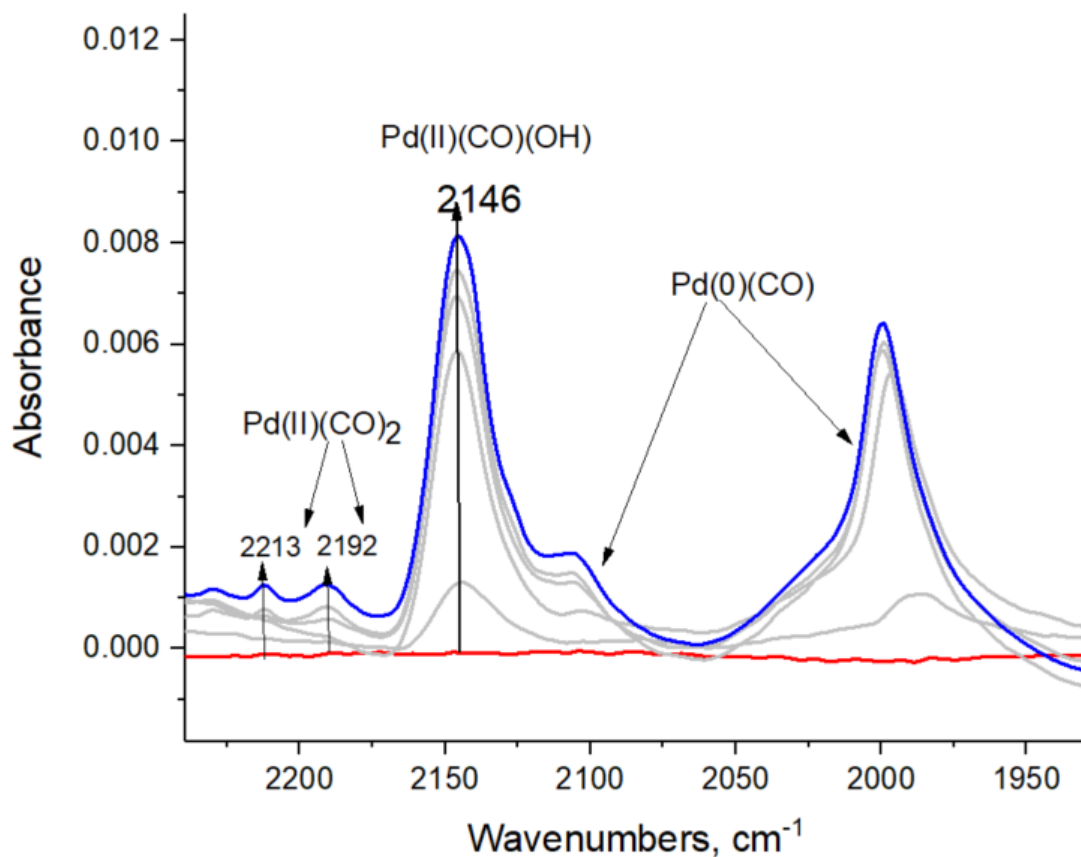
Figure S33. FTIR spectra during 5 Torr CO adsorption on 1 wt% Pd/SSZ-13 with Si/Al=30. Consistent with our previous work, Pd(II)(CO)2 are not stabilized selectively because at this Si/Al ratio with between 1 to 2 Al atoms per unit cell the fraction of paired Al T-sites in the vicinity is small. The major species is Pd(II)(CO)(OH) and a significant fraction of linear CO adsorbed on metal Pd(0) clusters and particles can be seen, consistent with findings in our Angew. Chem. Paper (ref. 8 main text) where HADDF-STEM and PNA performance testing show that for 1 wt% Pd/SSZ-13 sample with Si/Al~30 the amount of atomically dispersed Pd is ~30%, the rest is PdO nanoparticles and clusters.
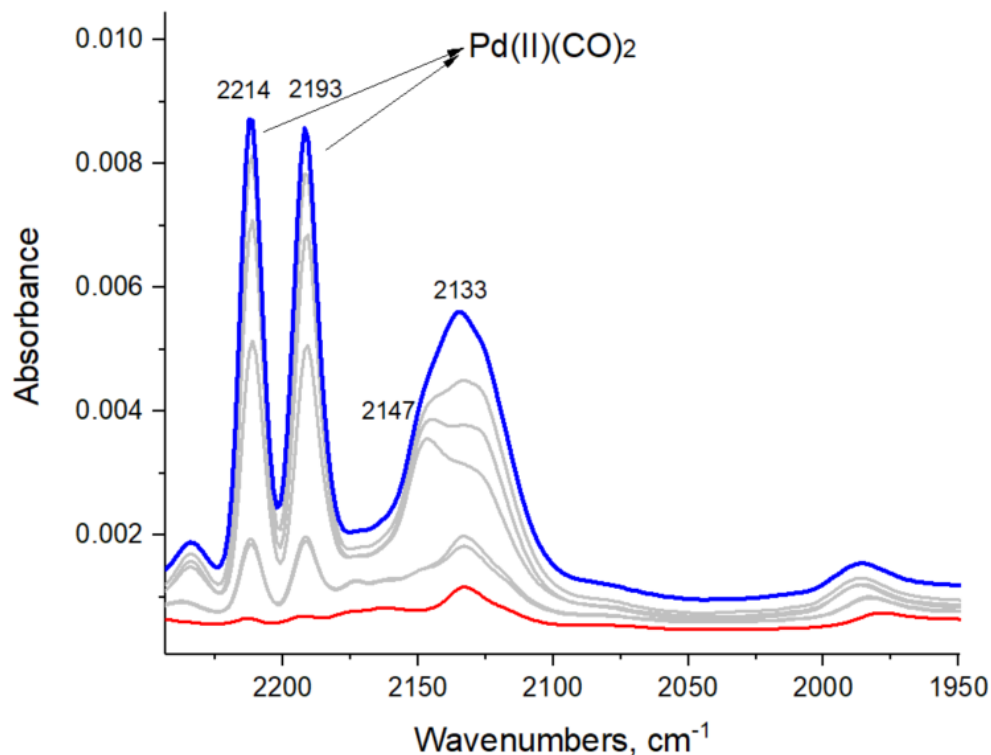
Figure S34. FTIR spectra during 5 Torr CO adsorption on 1 wt% Pd/SSZ-13 with Si/Al=12. $Pd(II)(CO)_2$ are formed with relatively high selectivity in addition to various Pd(II)(CO)(OH) species highlighting the abundance on nearby Al pairs in SSZ-13 with Si/Al ~12 (approx 3-4 Al T-sites per unit cell). Note however that for 1 wt% Pd/SSZ-13 with Si/Al 6 $Pd(II)(CO)_2$ is formed completely selectively (>95%) whereas for this sample with lower Al content a significant fraction of Pd(II)(CO)(OH) (2147-2133 cm^{-1} bands) and a minor fraction of CO adsorbed linearly on metallic Pd clusters can be seen as well. Thus, in our 1 wt% Pd/SSZ-13 Si/Al Pd selectively goes to Pd(II)/2Al sites.
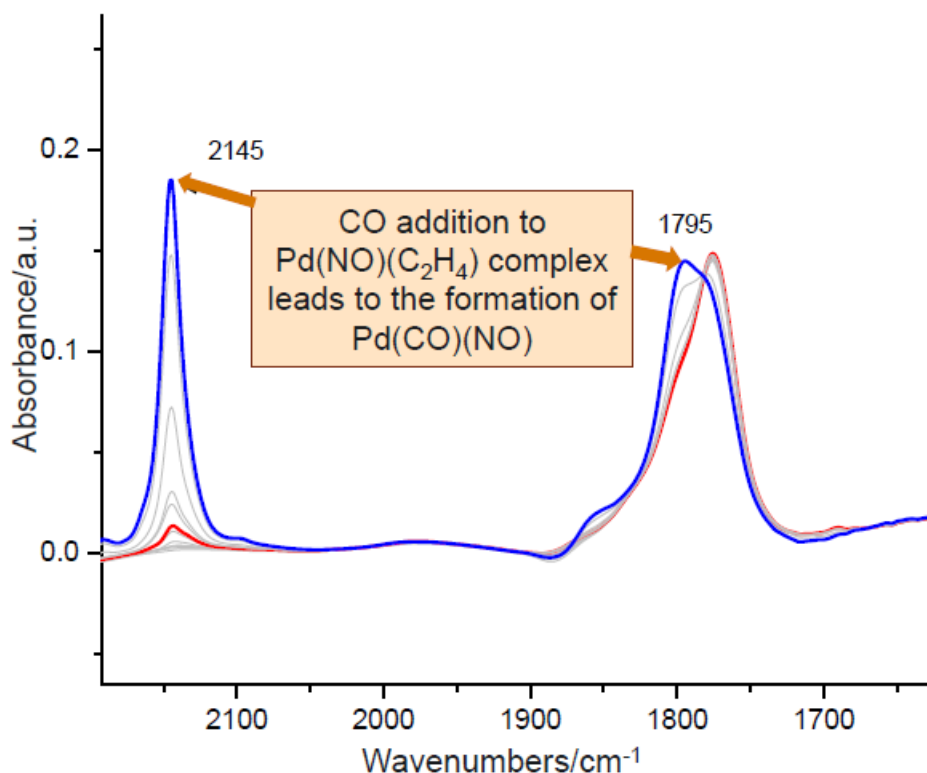
Figure S35. FTIR spectra during 0.5 Torr CO adsorption on Pd(NO)(C$_2$H$_4$) complex. CO is theoretically able to react with Pd(NO)(C$_2$H$_4$) the following pathways:

Pd(NO)(C$_2$H$_4$) + CO → Pd(CO)(C$_2$H$_4$) + NO   ***pathway 1***

Pd(NO)(C$_2$H$_4$) + CO → Pd(CO)(NO) + C$_2$H$_4$ ***pathway 2***

These data provide important information on ligand binding to Pd(II) in various mixed CO, NO and Ethylene containing Pd(II) complexes in zeolite. It is clear that pathway 2 is operative in excellent with binding energies of neutral ligands obtained in our DFT calculations (***Table S1***), showing higher stability of Pd(II)(CO)(NO) compared with Pd(II)(NO)(C$_2$H$_4$).
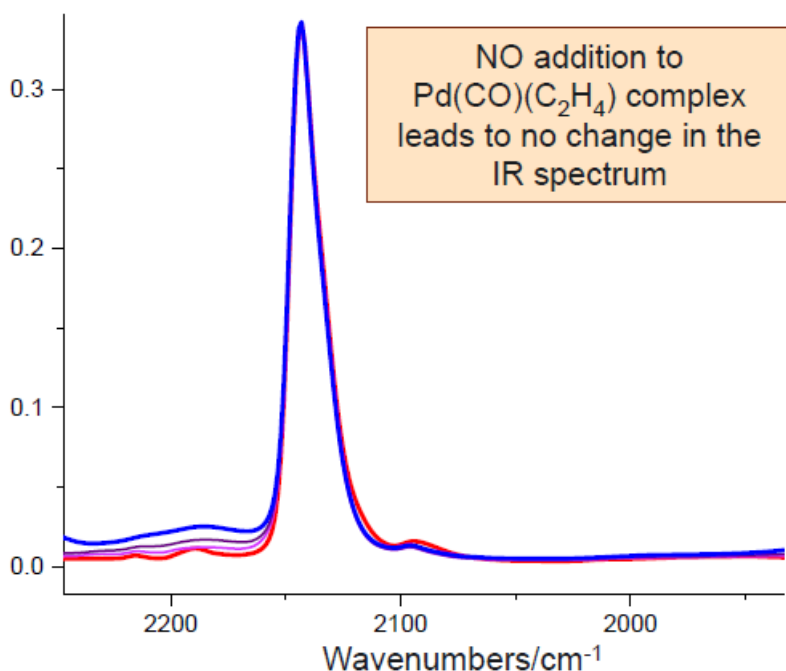
Figure S36. FTIR spectra during 0.5 Torr NO adsorption on Pd(CO)(C$_2$H$_4$) complex. NO is theoretically able to react with Pd(CO)(C$_2$H$_4$) the following pathways:

Pd(CO)(C$_2$H$_4$) + NO → Pd(NO)(C$_2$H$_4$) + CO   ***pathway 1***

Pd(CO)(C$_2$H$_4$) + NO → Pd(CO)(NO) + C$_2$H$_4$ ***pathway 2***

It is clear that Pd(II)(CO)(C$_2$H$_4$) is more stable than Pd(II)(NO)(C$_2$H$_4$) and Pd(II)(CO)(NO), therefore no ligand exchange takes place in agreement with our DFT calculations (***Table S1***). Thus, the row of mixed ligand binding can be constructed in terms of stability of produced complexes: Pd(CO)(C$_2$H$_4$) > Pd(CO)(NO) > Pd(NO)(C$_2$H$_4$).